Award Number: 05HQGR0031

GROUND MOTION ATTENUATION RELATIONS FOR THE INTERMOUNTAIN WEST

FINAL REPORT

AUGUST 15, 2006

N. Collins, R. Graves, G. Ichinose, and P. Somerville*

URS Group, Inc.

566 El Dorado Street
Pasadena, CA 91101

Tel: (626) 449-7650
Fax: (626) 449-3536

*Email: paul_somerville@urscorp.com

Research supported by the U.S. Geological Survey (USGS), Department of the Interior, under award number 05HQGR0031. The views and conclusions contained in this document are those of the authors and should not be interpreted as necessarily representing the official policies, either expressed or implied, of the U.S. Government.

GROUND MOTION ATTENUATION RELATIONS FOR THE INTERMOUNTAIN WEST

ABSTRACT

We have developed a strong ground motion model for earthquakes in the Intermountain West using a strong motion simulation procedure. The strong motion simulations use earthquake source parameters and scaling relations that are consistent with the source parameters of Basin and Range earthquakes, and Green's functions that are calculated from known crustal structure models of the Intermountain West. The ground motions are for a shear wave velocity of 0.76 km/sec (NEHRP S_B/S_C boundary), corresponding to soft rock and very stiff soil site conditions, which is the reference site condition used in the USGS National Seismic Hazard Maps. We developed models for horizontal ground motions for strike-slip and normal faulting earthquakes. The ground motions for strike-slip earthquakes and for non-hanging wall motions for normal faulting earthquakes are represented by the same model. There is a separate model for hanging wall motions for normal faulting at closest distances less than 20 km. The strike-slip model is defined for moment magnitudes up to 8, and the normal faulting models are defined for moment magnitudes up to 7.5. The ground motion models have short-period magnitude saturation at magnitude 7.0. They show a strong hanging wall effect that decreases with increasing magnitude. The ground motions have high long period amplitudes at close distances from large earthquakes, reflecting forward rupture directivity effects. We have not attempted to incorporate the spatial dependence of ground motion amplitudes on rupture directivity effects using parameters such as site location with respect to the hypocenter and fault geometry.

REVIEW OF EXISTING GROUND MOTION ATTENUATION MODELS

Three methods have been used to develop ground motion models for the Intermountain West. Empirical ground motion prediction models are derived from the regression analysis of recorded strong motion data (Abrahamson and Shedlock, 1997). At present the Spudich et al. (1999) ground motion model is the only empirical ground motion model that has been derived specifically for use in the Intermountain West. This model is based on a set of strong motion recordings from extensional tectonic environments. About two-thirds of the data were recorded in the southwestern United States and the remainder in other countries, mostly Italy.

The Spudich et al. (1999) model has two significant limitations. First, the magnitude scaling of this model is based not on the extensional data, but on a model derived from mostly California data (Boore et al., 1993), because the extensional data alone did not contain enough recordings of large earthquakes to constrain the magnitude scaling of the model. Second, it is not clear that data from other extensional regimes, which make up one-third of the data and most of the large magnitude data used in Spudich et al. (1999), are applicable to the Intermountain West. These limitations in the Spudich et al. (1999) model are reflected in the fact that, in generating the USGS National Seismic Hazard Maps for the Intermountain West (Frankel et al., 2000), the Spudich et al. (1999) model was given a weight of only 0.2, and the remaining weight of 0.8 was given to four ground motion models based mainly on California data. In view of the sparsity of recorded strong motion data in the Intermountain West, and the uncertainties entailed in the ground motion models in current use for this region, there is a need for more region-specific ground motion models for the Intermountain West.

There are two main alternative approaches to developing ground motion models for the Intermountain West. One approach is to modify models derived mostly from California data for differences in source, path and site characteristics between California and the Intermountain West. The application of this approach to the Yucca Mountain site was described by Stepp et al. (2001). In this approach, approximate adjustment factors are derived to account for differences in

source, path and site properties and applied to the California-based ground motion models. The ground motion experts who participated in the Yucca Mountain study tended to use lower stress parameter values, higher crustal Q values, and lower site attenuation (Kappa) values for Yucca Mountain than for California.

A second alternative approach, also used in the Yucca Mountain studies and which we have used in this project, is to perform broadband strong motion simulations using earthquake source, wave propagation path, and site attenuation models that are specific to the Intermountain West. This approach has the advantage of directly modeling the ground motions using region-specific characteristics, rather than attempting to adjust for regional differences in these characteristics. This procedure has been used extensively in the development of ground motion models in regions where recorded strong ground motions are too sparse to permit the development of empirical models. In a recently completed USGS project, we developed ground motion attenuation relations for the central and eastern United States (Somerville et al., 2001). These ground motion attenuation relations were used, along with others, to generate the 2000 and 2003 versions of the U.S. National Seismic Hazard Maps (Frankel et al., 2000).

APPROACH

Our approach consists of three steps. The first step is to develop earthquake source models and crustal structure models for use in generating ground motions. The source models are based on magnitude-area scaling relations for shallow crustal earthquakes in extensional tectonic regions, and on stress parameter values derived from these earthquakes. These stress parameter values are based on crustal structure models derived from the inversion of long period regional seismograms. The second step is to generate suites of ground motion time histories using these source models and crustal structure model. The third step is to use the ground motion simulations to develop the ground motion model.

HYBRID BROADBAND SIMULATION PROCEDURE

Our hybrid broadband strong motion simulation procedure (Graves and Pitarka, 2004) has a rigorous basis in theoretical and computational seismology, and uses the elastodynamic representation theorem and Green's functions. The earthquake source is represented as a shear dislocation on an extended fault plane, whose radiation pattern, and its tendency to become subdued at periods shorter than about 0.5 sec, are accurately represented. Wave propagation is represented rigorously by Green's functions computed for the seismic velocity structure which contains the fault and the site. These Green's functions contain both body waves and surface waves. The ground motion time history is calculated in the time domain using the elastodynamic representation theorem. This involves integration over the fault surface of the convolution of the slip time function on the fault with the Green's function for the appropriate depth and distance.

To simulate broadband time histories, the ground motions are computed separately in the short period and long period ranges, and then combined into a single broadband time history (Somerville et al., 1996; Graves and Pitarka, 2004). The use of different methods in these two period ranges is necessitated by the observation that ground motions have fundamentally different characteristics in these two period ranges. At long periods (longer than about 1 second), strong ground motions are deterministic in the sense that seismological models are capable of matching not only the spectral amplitudes but also the waveforms of recorded long period ground motions, once the rupture model of the earthquake and the seismic velocity structure of the region surrounding the earthquake are known. At short periods (shorter than about 1 second), strong ground motions become increasingly stochastic in nature. Seismological models are generally capable of matching the spectral amplitudes of the short period ground motions, but are generally not capable of matching the recorded waveforms. The transition from deterministic to stochastic behavior appears to be due to a transition from coherent source radiation and wave propagation

conditions at long periods to incoherent source radiation and wave propagation conditions at short periods.

We have developed and tested simple kinematic representations of the differences in source parameters, such as slip velocity and rupture velocity, between the shallow and deep parts of the rupture that are able to reproduce the observed differences in peak velocity and deep faulting earthquakes, using the broadband simulation procedure of Graves and Pitarka (2004). These differences are consistent with a trend for increasing stress drop in Basin and Range earthquakes described below in Figure 9. We use a slip velocity function that is constructed using two triangles as shown in Figure 1. This functional form is based on results of dynamic rupture simulations (Guatteri et al., 2003). We constrain the parameters of this function as follows:

$$T_r = 1.6 \times 10^{-9} \cdot M_0^{1/3} \quad depth < 5km$$

$$T_r = 3.2 \times 10^{-9} \cdot M_0^{1/3} \quad depth > 5km$$

$$T_p = 0.2 \cdot T_r$$

$$h = 0.2 \cdot A$$

where M_0 is the seismic moment, T_r is the rise time and A is normalized to give the desired final slip. The expression for T_r comes from the empirical analysis of Somerville et al. (1999). In general, T_r may vary across the fault; however, in practice we only allow a depth dependent scaling such that T_r increases by a factor of 2 if the rupture is between 0 and 5 km depth. This is consistent with observations of low slip velocity on shallow fault ruptures (Kagawa et al., 2004).

The rupture initiation time (T_i) is determined using the expression

$$T_i = R / V_r - \delta t$$

$$V_r = 0.8 \cdot V_s$$

where R is the rupture path length from the hypocenter to a given point on the fault surface, V_r is the rupture velocity and is set at 80% of the local shear wave velocity (V_s), and δt is a timing perturbation that scales linearly with slip amplitude such that $\delta t = \delta t_0$ where the slip is at its maximum and $\delta t = 0$ where the slip is at the average slip value. For these calculations, we set $\delta t_0 = 0.1 \sec$. This scaling results in faster rupture across portions of the fault having large slip as suggested by source inversions of past earthquakes (Hisada, 2001).

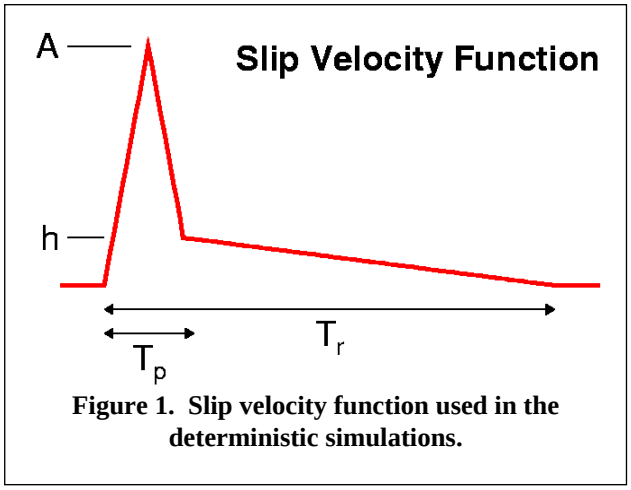

Figure 1. Slip velocity function used in the deterministic simulations.

We have made extensive tests of the ability of our broadband procedure to simulate the recorded strong ground motions of earthquakes. The goodness of fit between the estimated and actual ground motion parameters is quantified by measuring the difference in parameter values between the recorded and simulated ground motion time histories. An example of the testing and application of this simulation procedure is shown in Figure 2a, which compares the recorded (black) and simulated (red) velocity waveforms of the 1989 Loma Prieta earthquake at six stations. The amplitude and phasing of the recorded waveforms is generally well matched by the simulations.

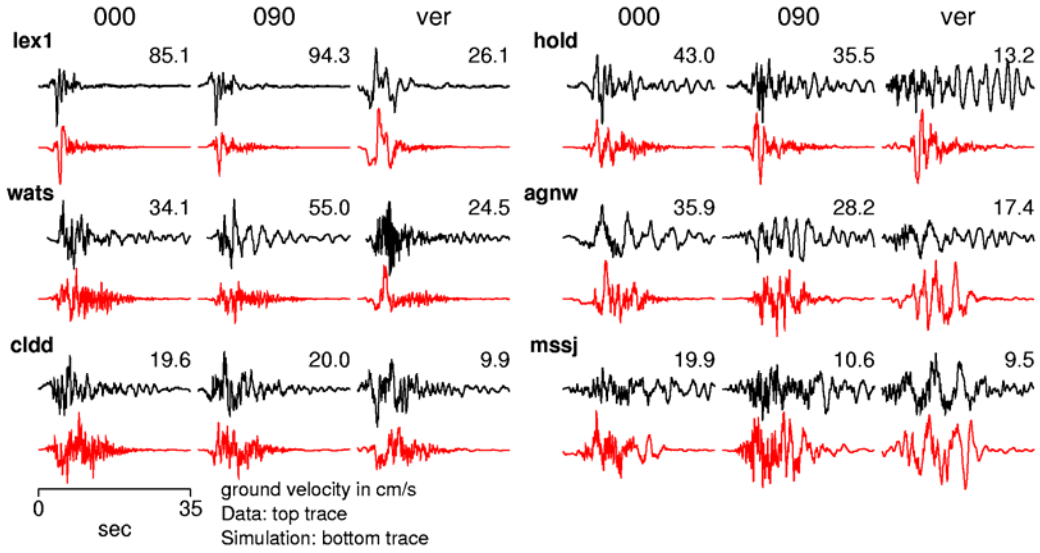

Figure 2a. Comparison of observed (black) and simulated (red) broadband 3-component ground velocity records at six sites for the Loma Prieta earthquake.

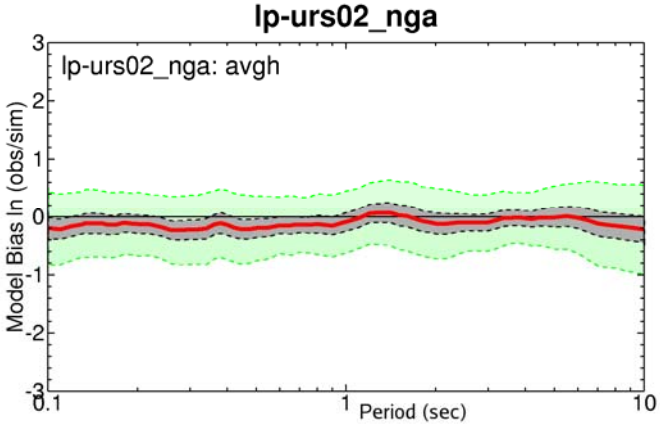

Figure 2b. Performance of the simulation procedure in matching the 5% damped response spectra of the 1989 Loma Prieta earthquake recorded at 21 stations. The red line shows the natural logarithm of the model bias (data – simulation) and the black dotted lines show its 90% confidence interval. The green lines show the natural logarithm of the standard error. Source: Graves and Pitarka, 2004.

The goodness of fit in spectral acceleration between the recorded and simulated time histories for 21 recordings of the 1999 Kocaeli earthquake is quantified in Figure 2b. This figure shows that the bias, i.e. median value of the residuals (data minus simulation) is not significant at the

90% confidence level. This means that averaged over all 21 stations, the simulation procedure neither over-predicts nor under-predicts the recorded ground motions. The standard error of the scatter of the individual residuals about this median value is shown on the right. The standard error of about a factor of 1.5 (0.4 natural log units) means that at a specific station, the difference between the recorded and simulation ground motion at a particular response spectral period has a standard error of a factor of 1.5.

The fundamental nature and the consequent predictive capability of this ground motion simulation approach was demonstrated at an early stage in the development of ground motion attenuation relations for the central and eastern United States. Burger et al. (1987) used simple wave propagation calculations in a horizontally layered crust to explain a flattening in the rate of attenuation that was observed in recordings of small earthquakes in this region. The following year, the effect of crustal structure on the attenuation of ground motion was more clearly demonstrated in the strong motion recordings of the 1988 Saguenay, Quebec earthquake (Somerville et al., 1990). At close distances (within about 50 km), the largest ground motions are caused by waves that travel upward from the earthquake source to the site. However, as distance from the source increases, the direct wave becomes weaker, and the reflections of downgoing waves from interfaces below the source reach the critical angle and undergo total internal reflection. The strong contrast in elastic moduli at these interfaces, especially the Moho, causes these critical reflections to have large amplitudes. The arrival of these critical reflections, beginning at a distance of about 50 km, causes a flattening of the attenuation relation out to distances of a few hundred km. The destructive potential of these effects was soon dramatically demonstrated in the 1989 Loma Prieta earthquake, in which major damage was done to buildings and bridges in the San Francisco Bay area located 80 to 90 km from the earthquake (Somerville et al., 1994).

The degree of flattening of the attenuation relation caused by the crustal waveguide, and the distance range over which it occurs, depend on the depth of the earthquake and the thickness and velocity profile of the crust. Consequently, ground motion attenuation characteristics will vary depending on the crustal structure and the depth of the earthquake. We have used earthquake depths and crustal structure models that are representative of the Intermountain West.

EARTHQUAKE RUPTURE DIMENSIONS IN THE INTERMOUNTAIN WEST

Procedures for characterizing earthquake sources in tectonically active regions for the simulation of strong ground motion were developed by Somerville et al. (1999), based on the rupture models of 15 crustal earthquakes. These rupture models were derived from the inversion of a combination of strong motion, teleseismic and geodetic data. The slip distributions of these events are highly variable, characterized by asperities (regions of large slip) surrounded by regions of low slip. These data were used to develop scaling relationships between seismic moment and a set of fault parameters that are needed for predicting strong ground motions, including fault length, fault width, rise time (duration of slip at a point on the fault), and the size, slip contrast and location of asperities.

Of the 15 earthquakes analyzed by Somerville et al. (1999), only one, the 1983 Borah Peak earthquake, was a normal faulting earthquake, and two others, the 1971 Imperial Valley and 1987 Superstition Hills earthquakes, were from extensional tectonic environments. The source scaling characteristics of these three earthquakes, including rupture area, average slip, size of regions having large slip (asperities), and distribution of slip with depth, are consistent with those of the other earthquakes in this data set. Using a much larger set of earthquakes, Wells and Coppersmith (1994) similarly found that the scaling of fault dimensions with magnitude for normal faulting earthquakes is similar to that of other earthquakes in tectonically active regions.

For this study, we analyzed the source dimensions of the larger historical earthquakes shown in Figure 3.

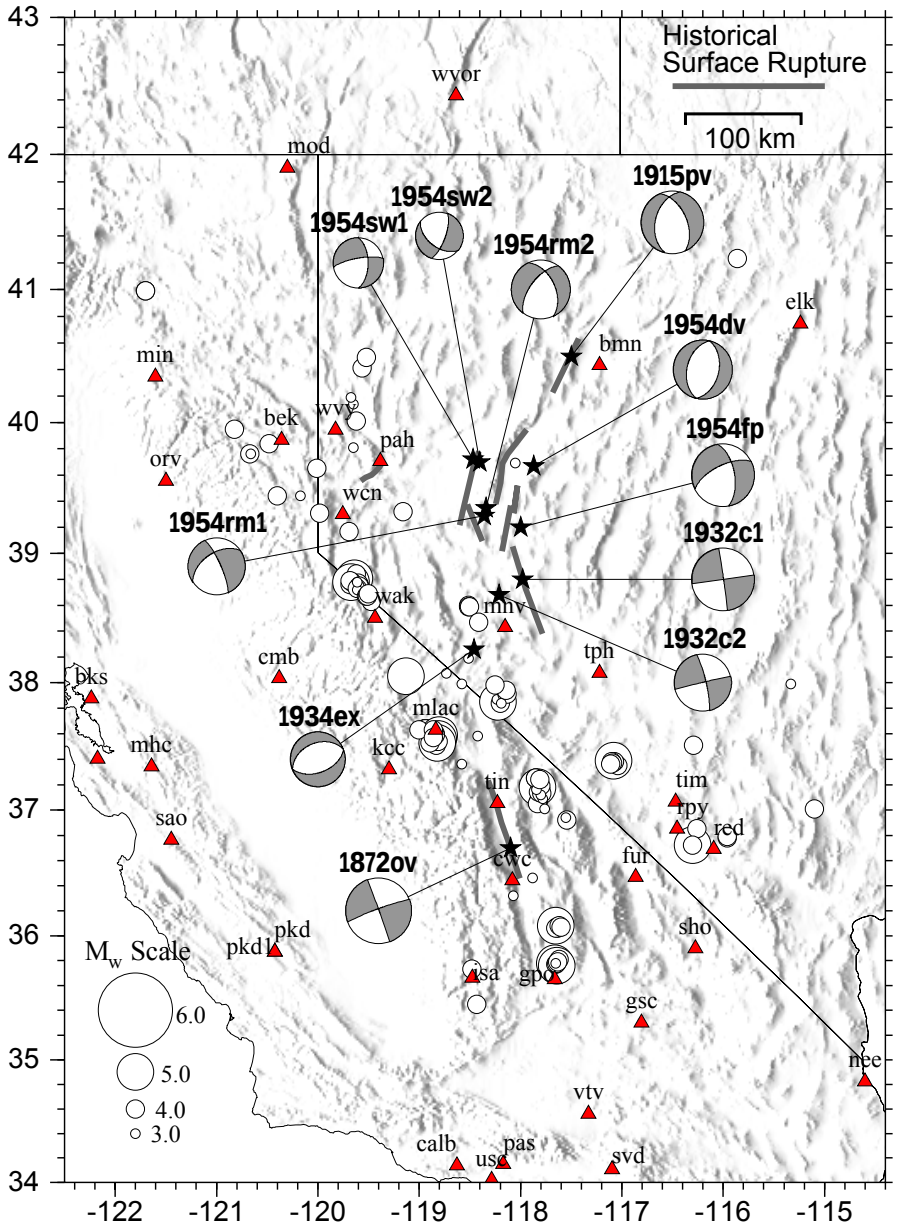

Figure 3. Approximate location of historical surface rupture earthquakes in eastern California and western Nevada.

In Figure 4, we show the fault dimensions and seismic moments of the five largest events (Mw 5.9 – 7.2) of the 1965-1959 Rainbow Mountain-Fairview Peak- Dixie Valley earthquake sequence (Doser, 1986), together with data from the Chalfant Valley sequence (Smith and Priestley, 2000), and the Round Valley (Priestley et al, 1998), Little Skull Mountain (Lohman et al., 2002) and Borah Peak earthquakes. The least squares fit to these data (solid line) is close to the relation of Somerville et al., 1999 (dashed line) for crustal earthquakes in tectonically active

regions. We conclude that the Somerville et al. (1999) scaling relations provide a reliable basis for characterizing the source dimensions of earthquakes in the Intermountain West for simulating strong ground motion.

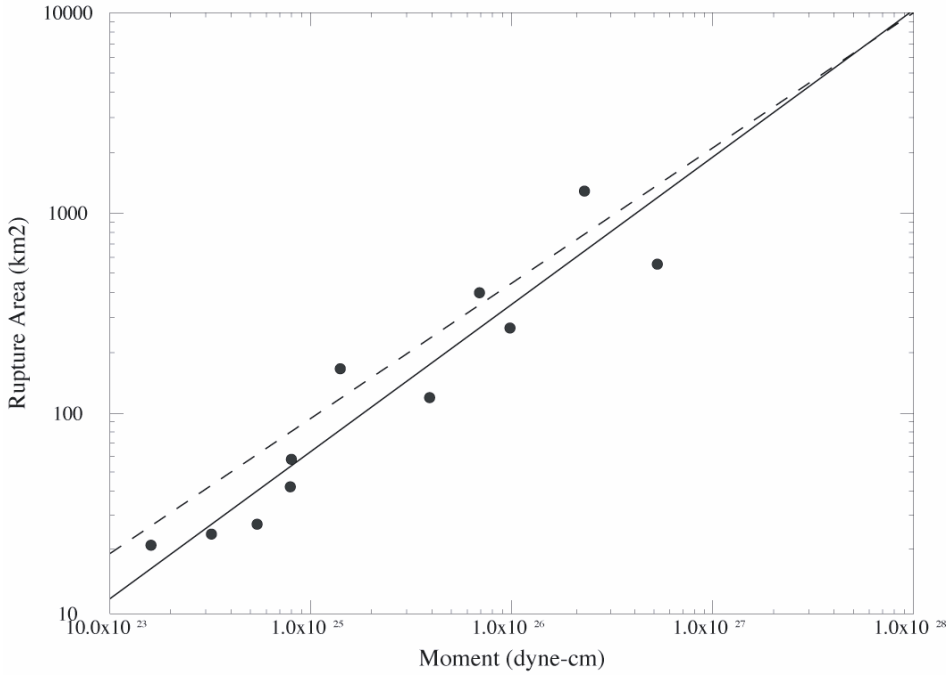

Figure 4. Scaling of rupture area with seismic moment for Basin and Range earthquakes. The solid line is the least-squares fit to the data, and the dashed line is the constant stress drop relation of Somerville et al. (1999) for crustal earthquakes in tectonically active regions.

CRUSTAL STRUCTURE AND SOURCE PARAMETERS IN THE INTERMOUNTAIN WEST

The short period component of the ground motion simulation procedure uses a stochastic method in which the seismic radiation from the fault is controlled by the stress parameter. Accordingly, we have used stress parameter values that are representative of Basin and Range earthquakes. We analyzed the source parameters of a large number of recent moderate magnitude Basin and Range earthquakes (Ichinose et al., 2003). The locations of these earthquakes, together with the focal mechanisms of larger, older earthquakes, are shown in Figure 5.

We took a comprehensive approach to the modeling or recorded S wave spectra in which we independently estimated the following parameters in sequence:

a) scalar seismic moment and radiation pattern from moment tensor inversion of long period waves; this fixes the low frequency spectral asymptote

b) frequency dependent path Q from S-wave and coda waves (scattering Qs and intrinsic Qi attenuation); this fixes the path Q for source spectral modeling

c) Assuming a geometrical spreading of $R^{-\eta}$ and $\omega^{-\eta}$, solve for static stress drop $\Delta\sigma$ and K. We then relate the static stress drop to the stress parameter used in the strong motion simulation procedure

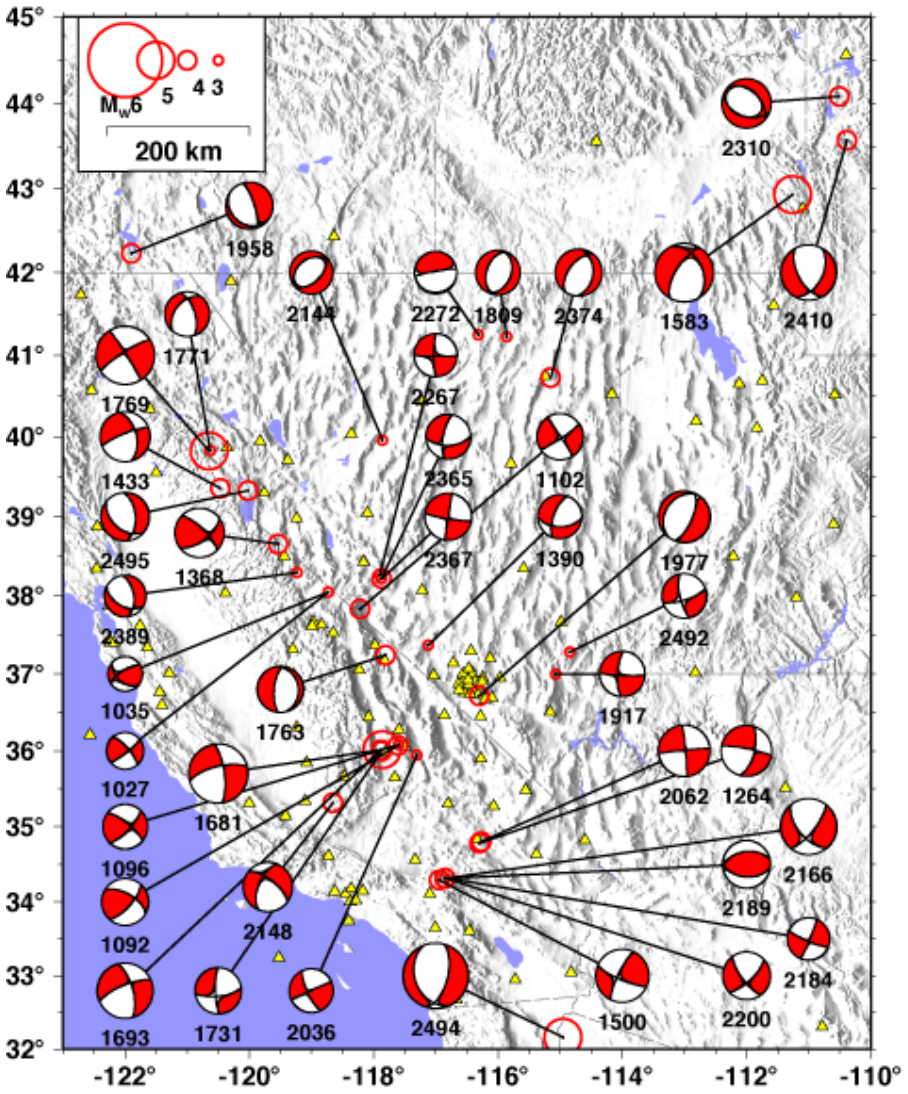

Figure 5. Approximate location of recent earthquakes (1990-2002) within eastern California and western Nevada modeled by Ichinose et al [2003] using the long period regional-wave moment tensor inversion method.

The fit of the Q model to the spectra of the September 20, 2004 Adobe Hills earthquake using this procedure is illustrated in Figure 6. The source parameters derived from the Adobe Hills earthquakes are shown in Figure 7. The source and path parameters resulting from these analyses are listed in Table 1.

Table 1. Source and Path Parameters of Basin and Range Earthquakes

Parameter	**Value**
Inelastic absorption	$Q(f) = 150\ f^{0.35}$
Geometrical spreading	$g\ (R) = R^{-1.3}$
Near surface absorption	$K = 0.05$
Static stress drop	$\Delta\sigma = 100$ bars

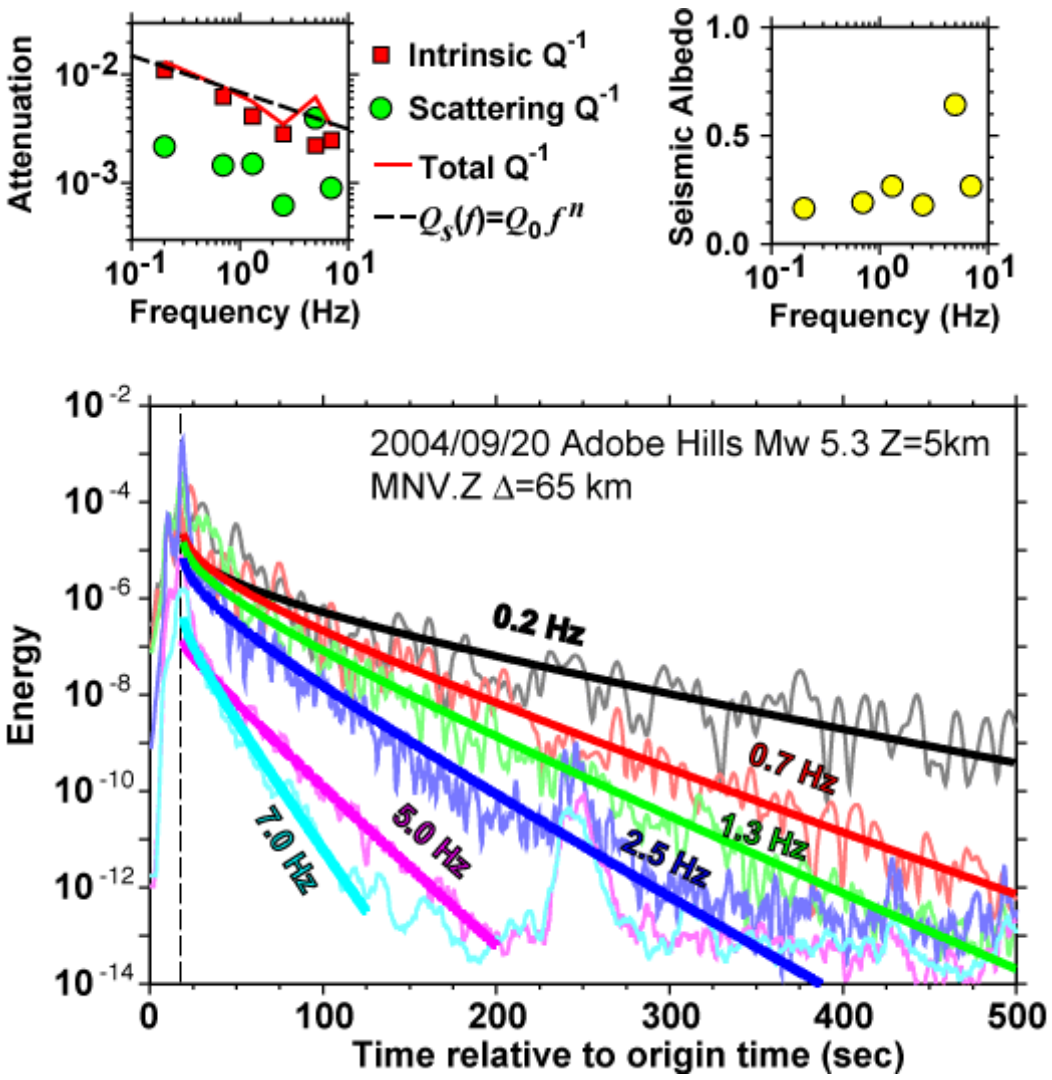

Figure 6. Fit of the Q model to the spectra of the September 20, 2004 Adobe Hills earthquake

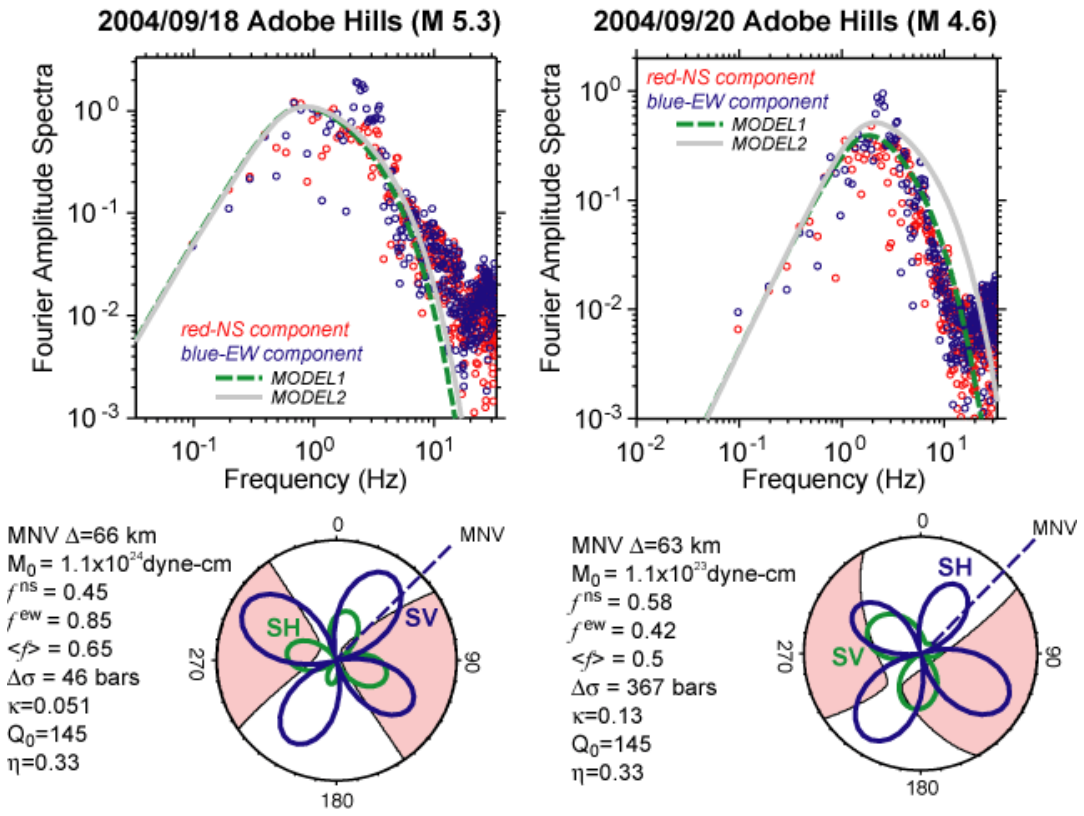

Figure 7. Source parameters derived from the Adobe Hills earthquakes

The source parameters of numerous Basin and Range earthquakes (Figure 4) measured using the procedure described above and listed in Table 2 are compared with compilations of other Basin and Range as well as other earthquakes (Ichinose et al., 2003) in Figure 8. Becker and Abrahamson (1997) found that the stress parameters of Basin and Range earthquakes are about three-quarters as large as the values for California earthquakes. From Figure 8 we conclude that there is no significant difference in stress parameters between Basin and Range earthquakes and California earthquakes.

Table 2. Source Parameters of Small Basin and Range Earthquakes

No.	Year Month Day Hour Min Place	Depth (km)	Seismic Moment (dyne*cm)	Static Stress Drop (bars)
1	20031123_1219_Elko	10	1.641e+22	127
2	20011008_0537_Elko	6	8.810e+21	280
3	20040920_1651_AdobeHills	5	1.096e+23	367
4	20040918_2302_AdobeHills	5	1.100e+24	50
5	20040603_0854_InclineVillage	10	2.239e+22	189
6	20030821_0746_Wyoming	6	2.951e+22	52
7	20040107_0751_Wyoming	11	2.042e+23	140
8	20020614_1240_LittleSkull	10	6.531e+22	31
9	20001202_1534_Truckee	14	3.89E+22	369
a	20010810_2019_Portola	20	8.41E+23	221
b	19981030_0953_InclineVillage	11	1.91E+23	119

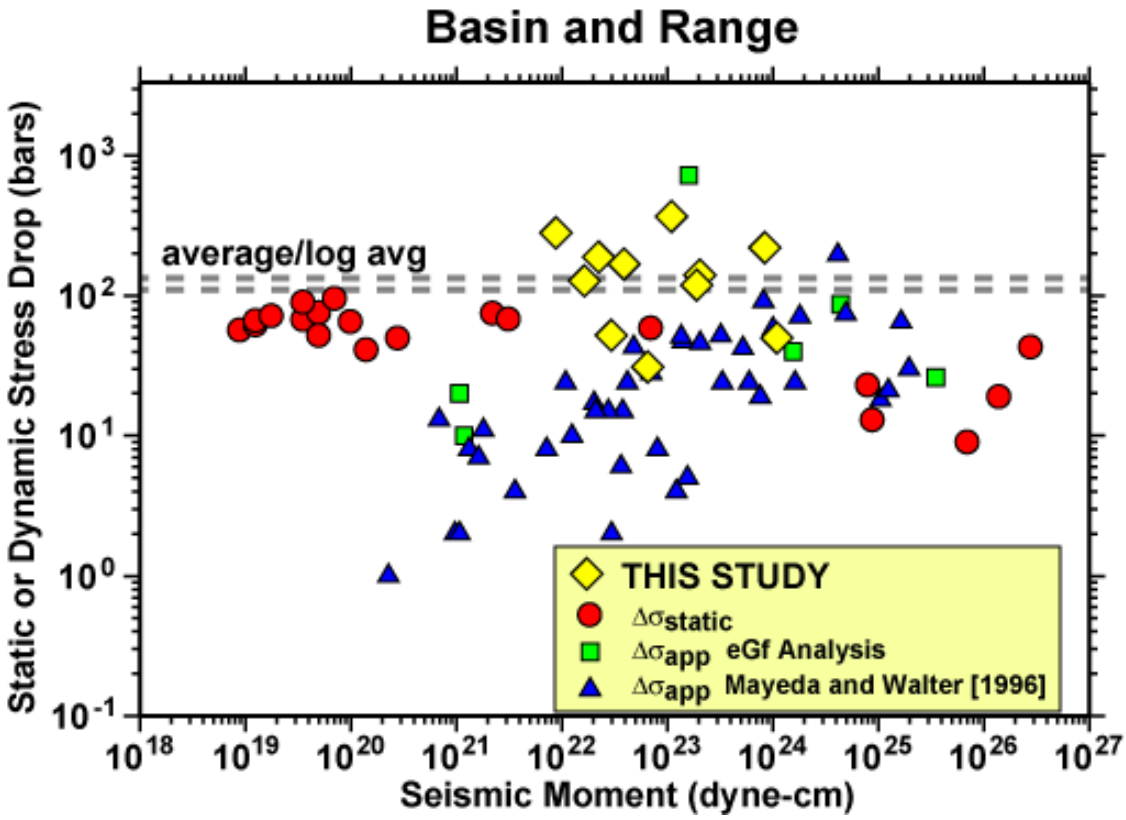

Figure 8. Apparent stress drop ($\Delta\sigma_{app}$) and static stress drop ($\Delta\sigma_{static}$) versus moment magnitude measured from earthquakes within the Basin and Range. Apparent stress measurements were made using P-wave pulse width (Priestley et al., 1988; Smith and Priestley, 2000), empirical Green's function analysis (Horton et al., 1997; Ichinose et al., 1999), and from radiated energy from S-wave Coda (Mayeda and Walter, 1996). Static stress drops were measured by Ichinose et al. (1997) and Hawkins et al. (1986) from S-wave spectral analysis and source inversion using teleseismic data by Doser (1986).

In Figure 9, we analyze the depth dependence of static stress drop in the earthquakes analyzed by Ichinose et al. (2003). The lines shown in Figure 9 were fitted after events 2 and 3 were excluded. These data suggest a linear increase of stress drop with depth, although event numbers 2 and 3 depart strongly from this trend. The trend of increasing stress drop with depth is consistent with the way in which we have modeled the slip velocity and rise time in the upper 5 km in our simulation procedure, described above.

Derivation of Stress Parameter Value from Static Stress Drop Estimates

The static stress drop values shown in Figures 8 and 9 were estimated following the methodology of Brune (1970). This approach relates the measured corner frequency and seismic moment to the static stress drop level from the Q – corrected spectra. In determining the seismic moment for these events, we applied corrections for radiation pattern and free-surface amplification effects. Since the moment values are determined from long period (T> 50 sec) data, the assumed velocity structure included gross shallow crustal layering (vp = 4.5 km/sec, vs = 2.0

km/sec, density = 2.39 gm/cc). On average, we found static stress drop levels of 100 bars, which is consistent with the value found for California using the same methodology.

In contrast, our broadband simulation methodology (Graves and Pitarka, 2004) uses a stress parameter to scale the high frequency radiation from each subfault. In the original formulation of Boore (1983), the role of this stress parameter was similar to the static stress drop described above. That is, the original formulation assumed 1/R Green's functions in a half-space velocity structure (with corrections for radiation pattern and free-surface). However, in our simulation methodology, we impose a 1D velocity structure and calculate ray Green's functions through this structure. These ray GFs include impedance amplification effects, which typically are about a factor of 2 at frequencies of 5 – 10 Hz (Boore and Joyner, 1997). Thus, in our approach, the high frequency scaling is affected not only by the assumed stress parameter, but also by the effects of impedance amplification. Based on the validation of our methodology against recorded strong motion data in California (Northridge and Loma Prieta), we fix the value of this stress parameter at 50. The factor of 2 difference between our simulation stress parameter and our static stress drop estimates is accounted for by the inclusion of impedance amplification in the simulation process.

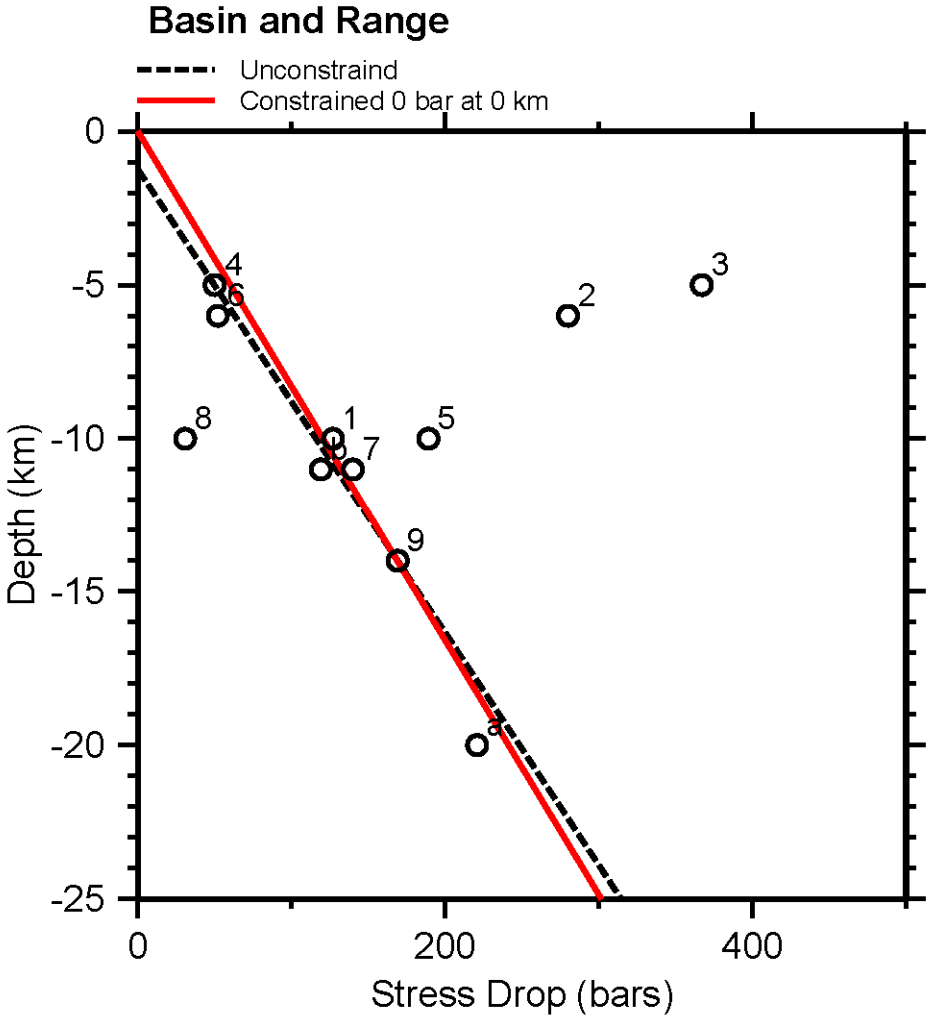

Figure 9. Dependence of static stress drop on depth in small Basin and Range earthquakes. The fit lines required the removal of outlier events 2 and 3.

Crustal Structure of the Intermountain West

The crustal structure of the Intermountain West has been extensively investigated (Pakiser, 1989; Smith et al., 1989; Thompson et al., 1989; Catchings and Mooney, 1991). We have found that a fairly simple crustal model with a crustal thickness of about 30 km is quite effective for modeling the long period waveforms of earthquakes in western Nevada and eastern California (Ichinose et al., 2003). In Figure 10, we show a profile of recordings of the 1998 Incline Village earthquake (Ichinose et al., 1999) that occurred at the western edge of the Basin and Range near the California border. The profile shows recordings in the Basin and Range and in California in the distance range of 10 to 1,000 km. The seismograms are compatible with the predicted arrival times of phases calculated from the Catchings and Mooney (1991) average crustal model along the NW-SE PASSCAL transect. The attenuation of peak velocity with distance for the Basin and Range stations is quite similar to that for the California stations (Figure 11).

Using recordings such as those shown in Figure 10, we inverted the seismic velocity structure from long period regional seismograms recorded along the paths shown in Figure 12 using the method described by Ichinose et al. (2005). Comparisons of recorded and simulated waveforms of the 2004 Incline Village earthquake and the Little Skull Mountain earthquake using the Basin and Range (BR) crustal model derived in this study are shown in Figures 13 and 14 respectively. The BR velocity structure model derived from these data is shown in Figure 15.

The Q model given above was incorporated into the layered model listed in Table 3. The surface layer of this model was assigned a shear wave velocity of 0.76 km/sec, consistent with the S_B/S_C boundary, which is the reference site condition used in the USGS National Seismic Hazard Maps.

Table 3. Layered Velocity Model for the Intermountain West

Thickness	P wave vel.	P wave Q	S wave vel.	S wave Q	Density
			0.76		
1.0	3.87	100	2.23	50	2.01
1.0	4.32	100	2.49	50	2.15
1.0	4.79	100	2.77	50	2.30
1.0	5.25	100	3.03	50	2.45
1.0	5.71	100	3.30	50	2.60
5.0	6.12	100	3.53	50	2.73
5.0	6.12	200	3.53	100	2.73
5.0	6.12	500	3.53	250	2.73
5.0	6.20	200	3.58	100	2.75
5.0	6.40	200	3.70	100	2.82
5.0	7.74	500	4.47	250	3.25
10.0	7.74	500	4.47	250	3.25
10.0	7.74	500	4.47	250	3.25
700.0	7.74	500	4.47	250	3.25

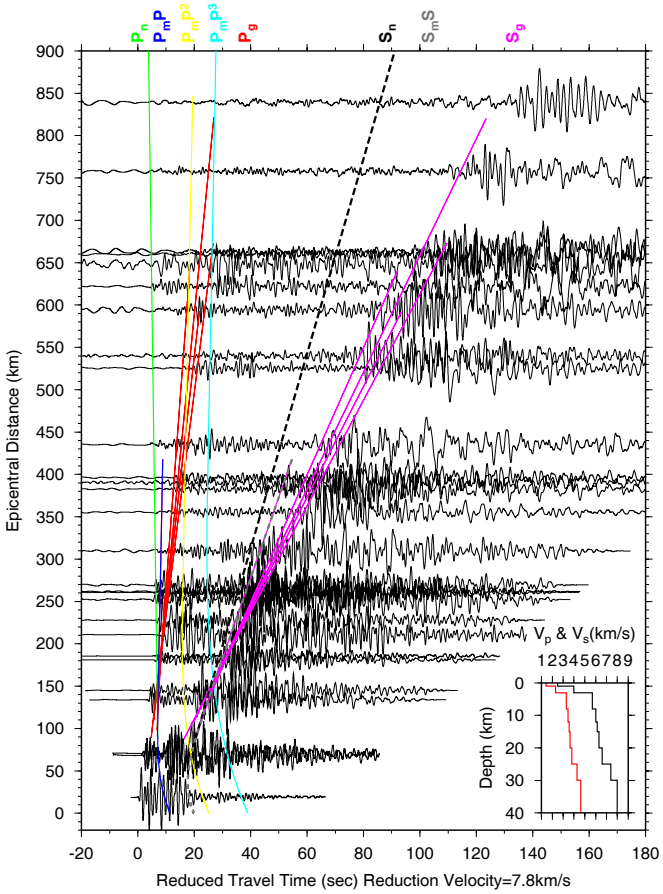

Figure 10. Record section of vertical component velocity seismograms from the 1998-10-30 Incline Village, Nevada (M_w 4.8) earthquake, with travel-times of various crustal phases computed from the Catchings and Mooney [1991] average velocity model of the NW-SE transect.

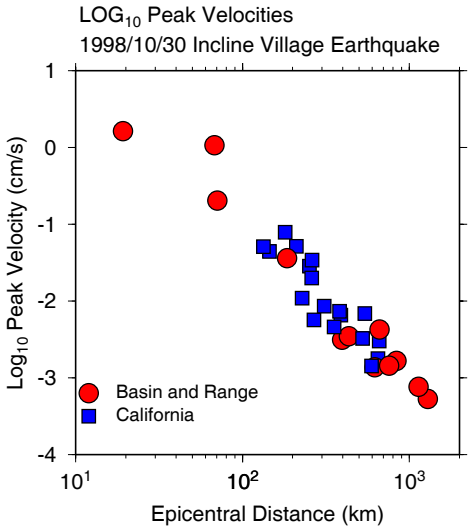

Figure 11. Maximum peak velocity versus epicentral distance measured from the M_w 4.8 Incline Village earthquake. Source and receiver paths crossing the Sierra Nevada into California are shown as squares and pure Basin and Range paths are shown as circles.

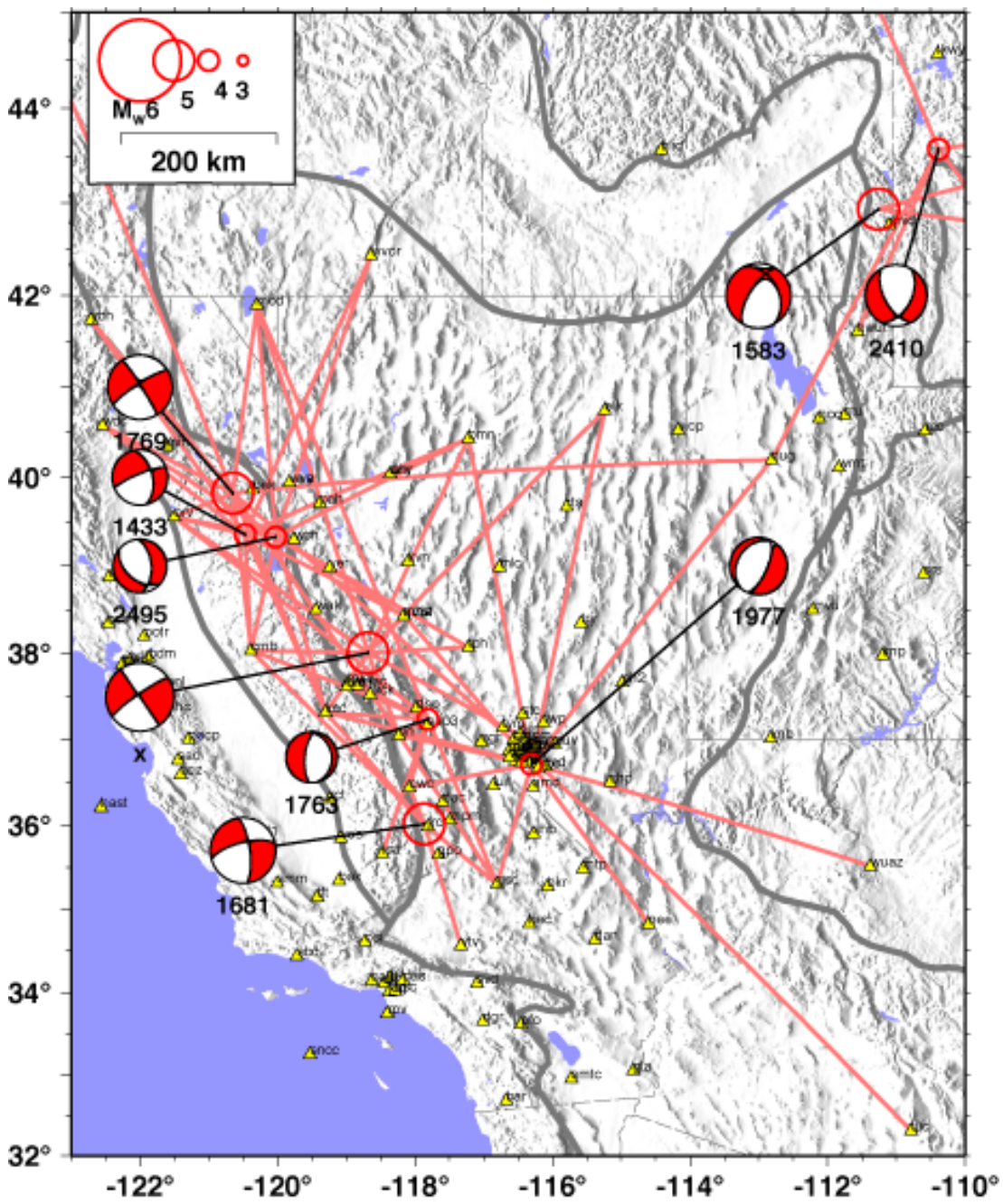

Figure 12. Paths between earthquakes and recording stations used in estimating crustal structure.

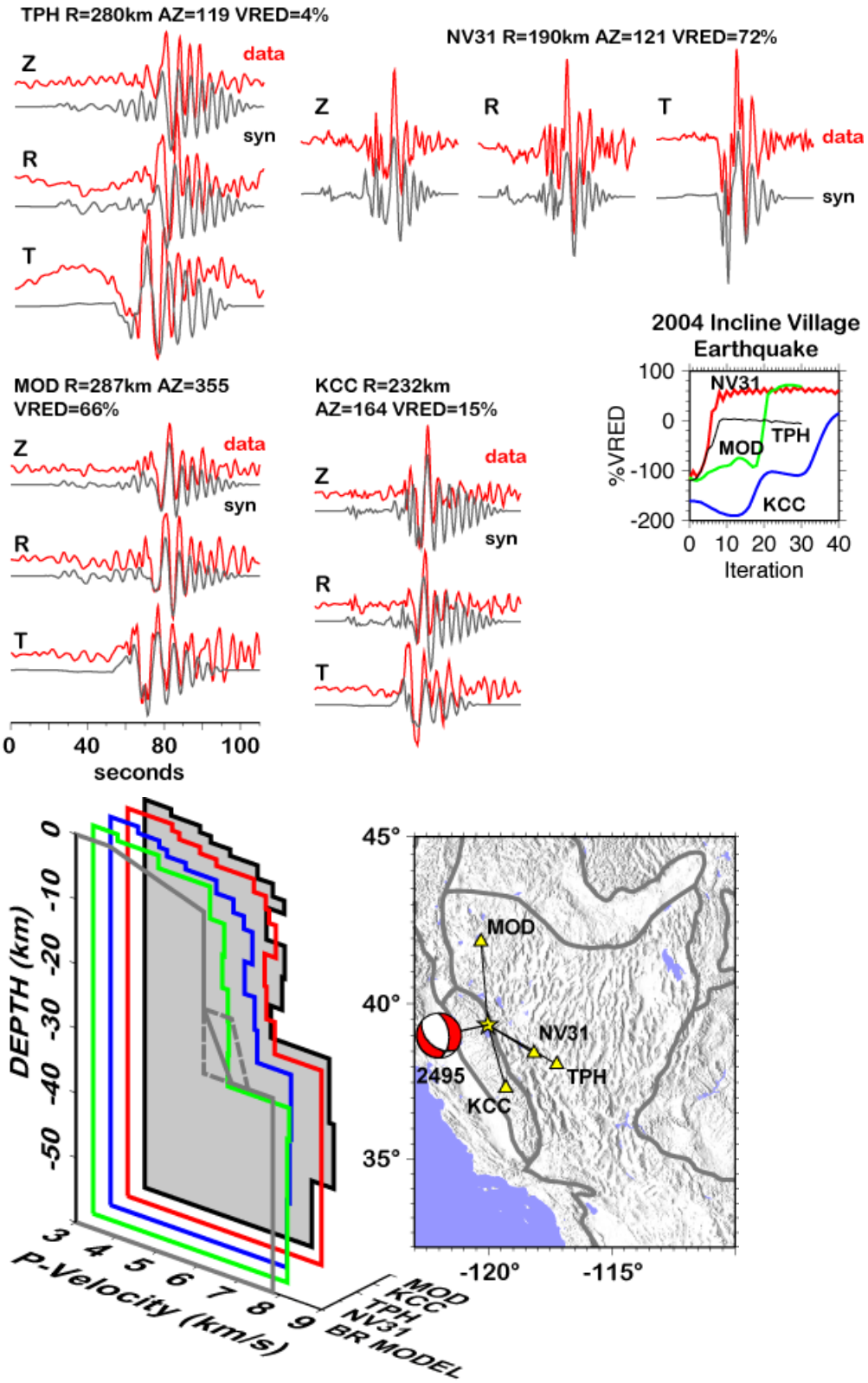

Figure 13. Top: Comparison of recorded and simulated waveforms of the 2004 Incline Village earthquake using the Basin and Range (BR) crustal model derived in this study. Bottom: Comparison of models derived from individual stations with the BR model.

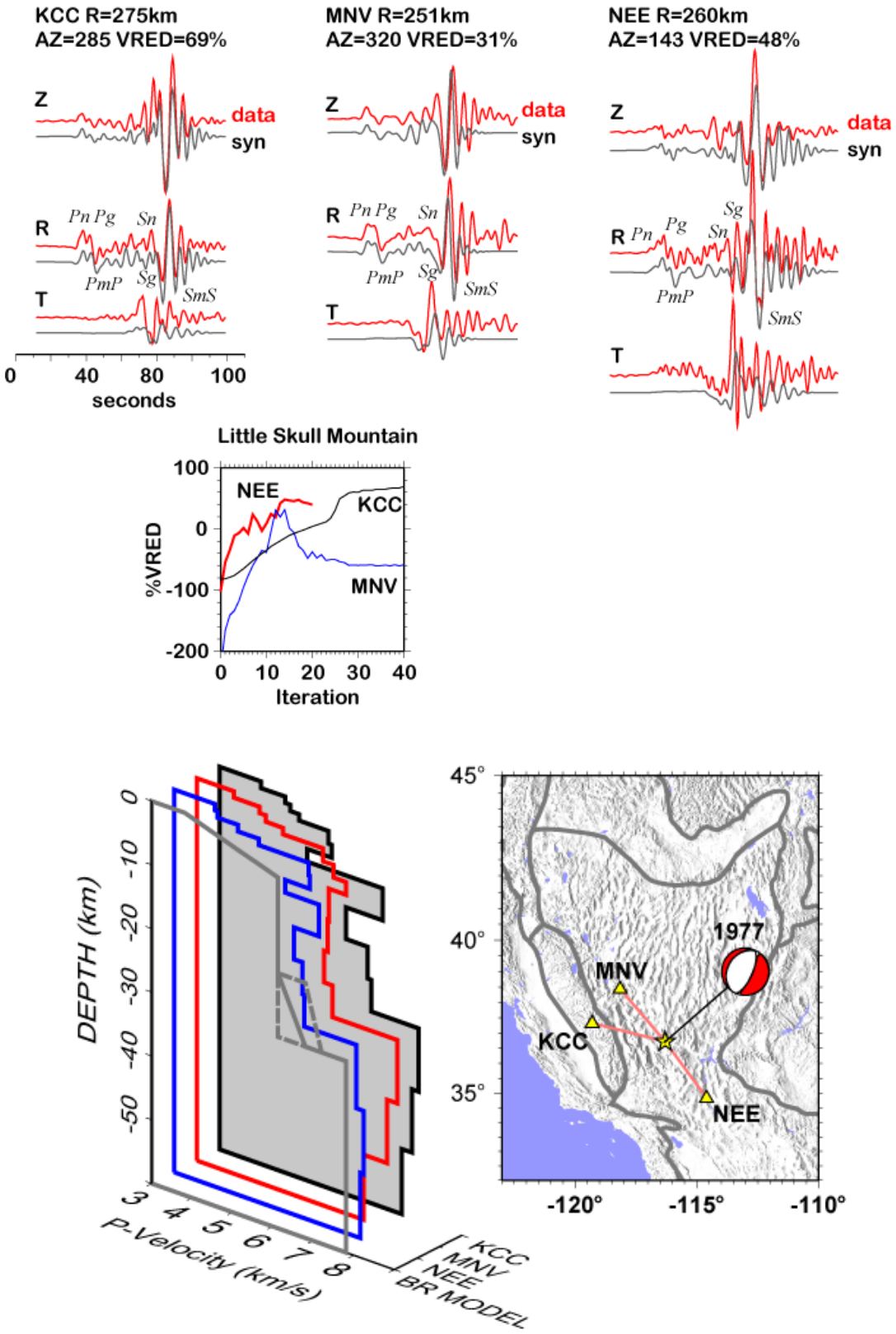

Figure 14. Top: Comparison of recorded and simulated waveforms of the Little Skull Mountain earthquake using the Basin and Range (BR) crustal model derived in this study. Bottom: Comparison of models derived from individual stations with the BR model.

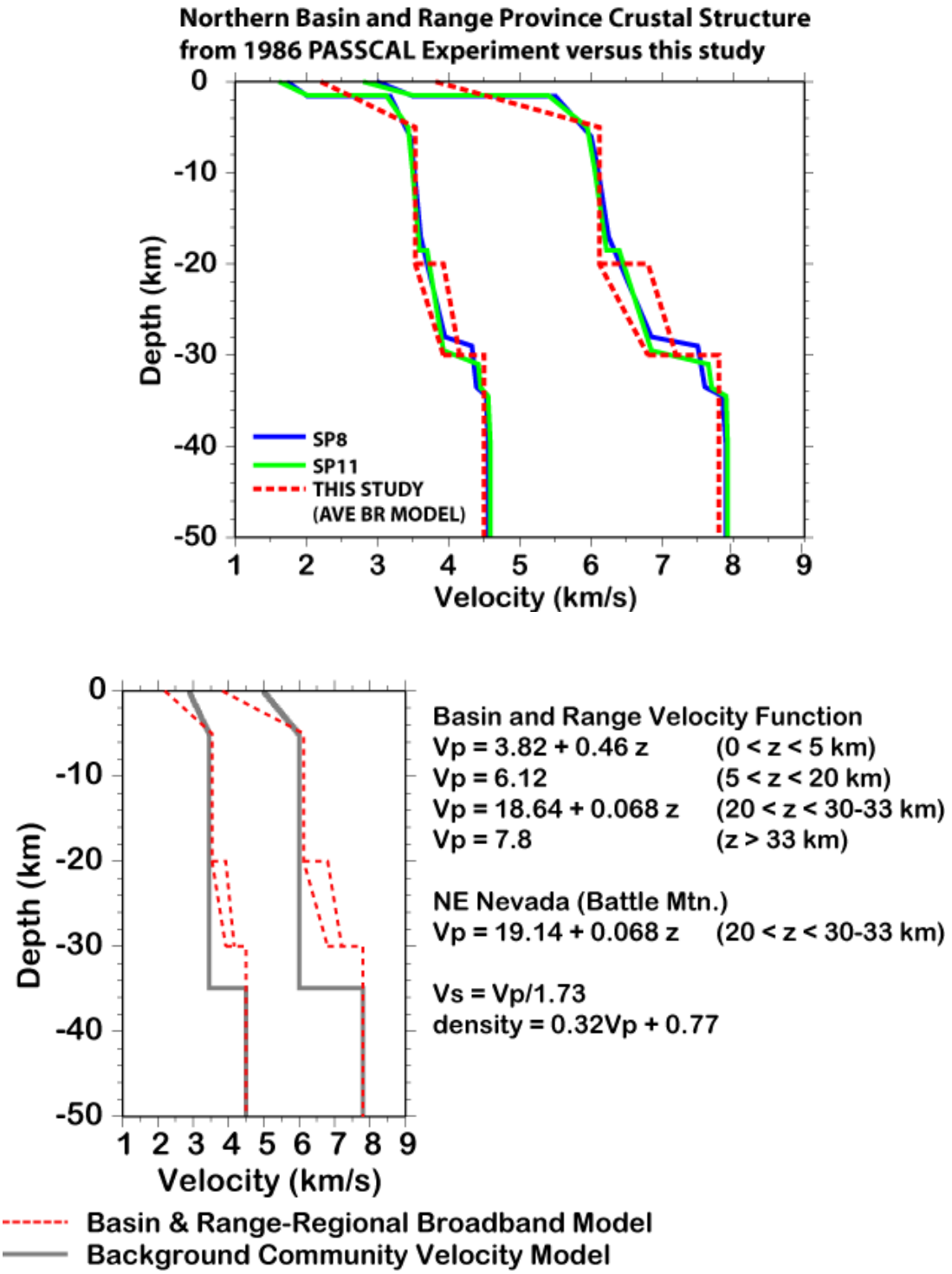

Figure 15. Top: Comparison of the Basin and Range (BR) crustal model derived in this study with other crustal models. We used the BR model having lower velocities in the depth range of 20 to 30 km.

SOURCE CHARACTERIZATION FOR STRONG MOTION SIMULATIONS

The ground motion attenuation model was derived from large suites of broadband simulations of ground motions. The ranges of magnitude, distance, frequency, and source parameters that were used are listed in Table 4.

Table 4. Parameterization of Ground Motion Models

PARAMETER	VALUE
Magnitude	Mw 6.5 - 7.5
Distance	0 - 200 km
Mechanism	Vertical strike-slip, Normal (60^o dip)
Crustal Structure	α, β, ρ, Q (h); K (Tables 1 and 3)
Site Condition	S_B/S_C boundary (Vs = 760 m/sec)
Rupture Area	Scaling relation (Figure 4)
Rupture Velocity	0.8 Vs
Stress Parameter	50 bars
Site Location (normal faults)	Foot wall; Hanging wall

The source dimensions of the faults used in the simulations are listed in Tables 5 and 6. For the strike-slip earthquakes, these are the same as used in the NGA-E strong motion simulations (Chiou et al., 2003; Somerville et al., 2003). For the normal faulting earthquakes, the dimensions are modifications of the reverse fault scenarios used in the NGA-E strong motion simulations, shown in parentheses in Table 6. The dip angle of 60^o and the maximum depth of 16.5 km are consistent with the values used for normal faults for the Intermountain West in the USGS National Seismic Hazard maps (Frankel et al., 2000). The average rupture velocity was assumed to be 0.8 Vs. We have assumed that, unlike conditions that pertain in California, all earthquakes in the Intermountain West having magnitudes of 6.5 and larger rupture the ground surface. Thus we do not expect large earthquakes in the Intermountain West to have the unusually strong ground motions that are associated with large earthquakes that do not break the ground surface, such as the 1989 Loma Prieta and 1994 Northridge earthquakes (Somerville and Pitarka, 2006).

Table 5. IMW Strike Slip Fault Scenarios (Same as NGA-E)

Event Name	Mag	Area (km^2)	Width (km)	Length (km)	Dip	Top of Rupture (km)
SA	6.5	325	13	25	90	0
SD	7.0	1005	15	67	90	0
SE	7.5	3150	15	210	90	0

Table 6. IMW Normal Fault Scenarios (modified from NGA-E reverse fault scenarios)

Event Name	Mag	Area (km^2)	Width (km)	Length (km)	Dip	Top of Rupture (km)
NE (RE)	6.5	323 (324)	17 (18)	19 (18)	60	0
NI (RI)	7.0	989 (988)	19 (23)	52 (43)	60	0
NK (RK)	7.5	3173 (3164)	19 (28)	167 (113)	60 (45)	0

Examples of the rupture models for the magnitude 7 strike-slip scenarios are shown in Figure 16. In all, we used 24 realizations of the rupture model for each scenario earthquake. The random spatial distribution of slip is based on empirically derived spatial frequency κ^{-2} distributions from the analysis of kinematic slip models (Somerville et al. 1999). Realizations include the variation of hypocenter location (deep and shallow, and along strike).

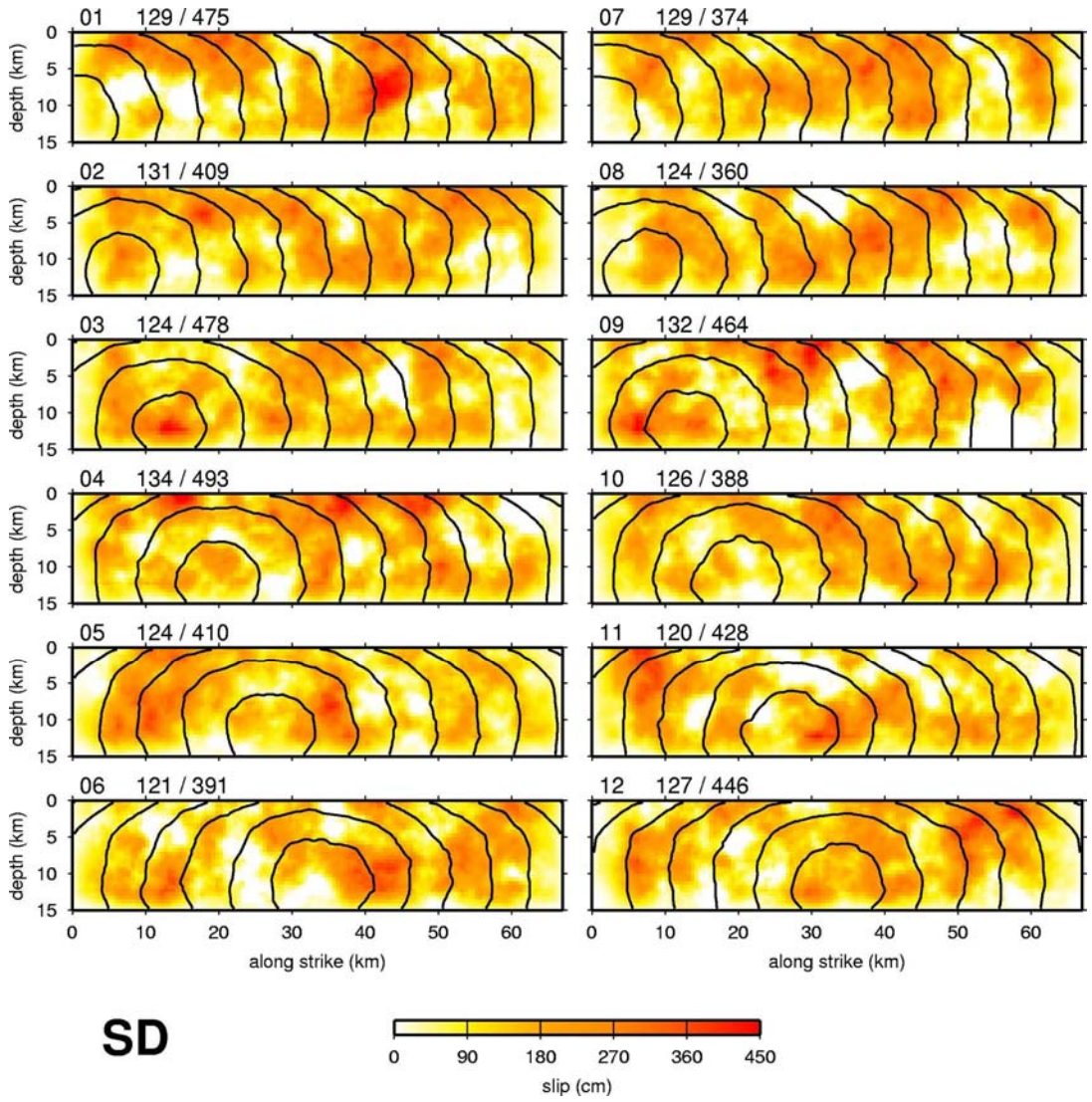

Figure 16. Distribution of slip and rupture time for 12 realizations of the Mw 7 strike-slip earthquake.

The station distribution used in the ground motion simulations is shown in Figure 17 for the magnitude 7.0 strike-slip earthquake, and in Figure 18 for the magnitude 7.0 normal faulting earthquake. The strike-slip station distribution is symmetrical about the fault, so only one side was simulated. The station set was designed to provide uniform spatial coverage within discrete ranges of distance to the surface projection of the fault. At close distances, the station spacing is 2 km, and has a nested pattern of thinning with increasing distance from the fault. The dense and uniform spacing and uniform site conditions that can be obtained using strong motion simulations are in marked contrast with those of the recorded strong motion data sets of most earthquakes.

The attenuation of the simulated ground motions for the magnitude 7 earthquake is shown for strike-slip faulting and non-hanging wall sites in normal faulting in Figure 19, and for hanging wall sites in normal faulting in Figure 20. Hanging wall sites are restricted to closest distances less than 20 km, and the two models merge at 20 km.

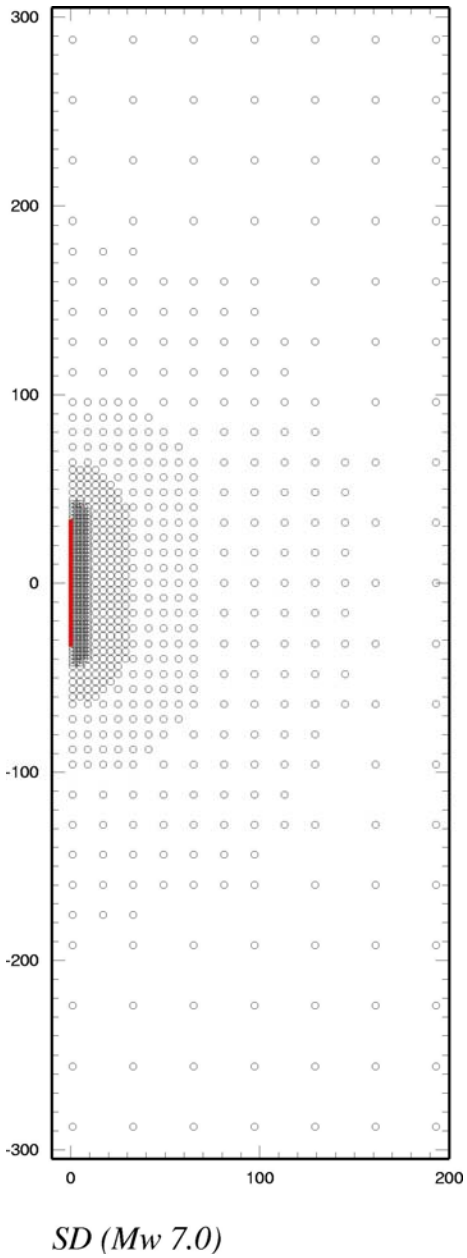

Figure 17. Station distribution for the magnitude 7.0 strike-slip earthquake. The top edge of the vertical fault is shown by the solid red line.

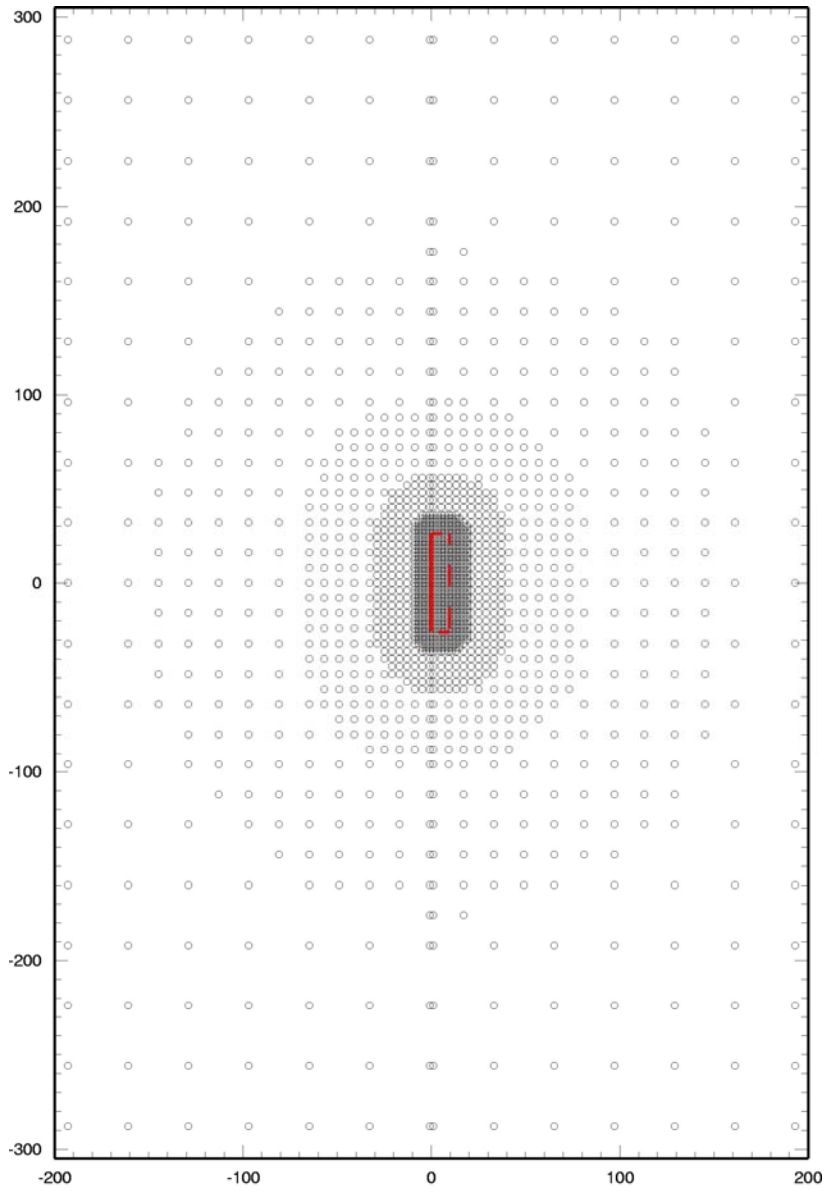

Figure 18. Station distribution for the magnitude 7.0 normal faulting earthquake. The top edge of the fault is shown by the solid red line, and the surface projection of the fault is shown by dashed lines.

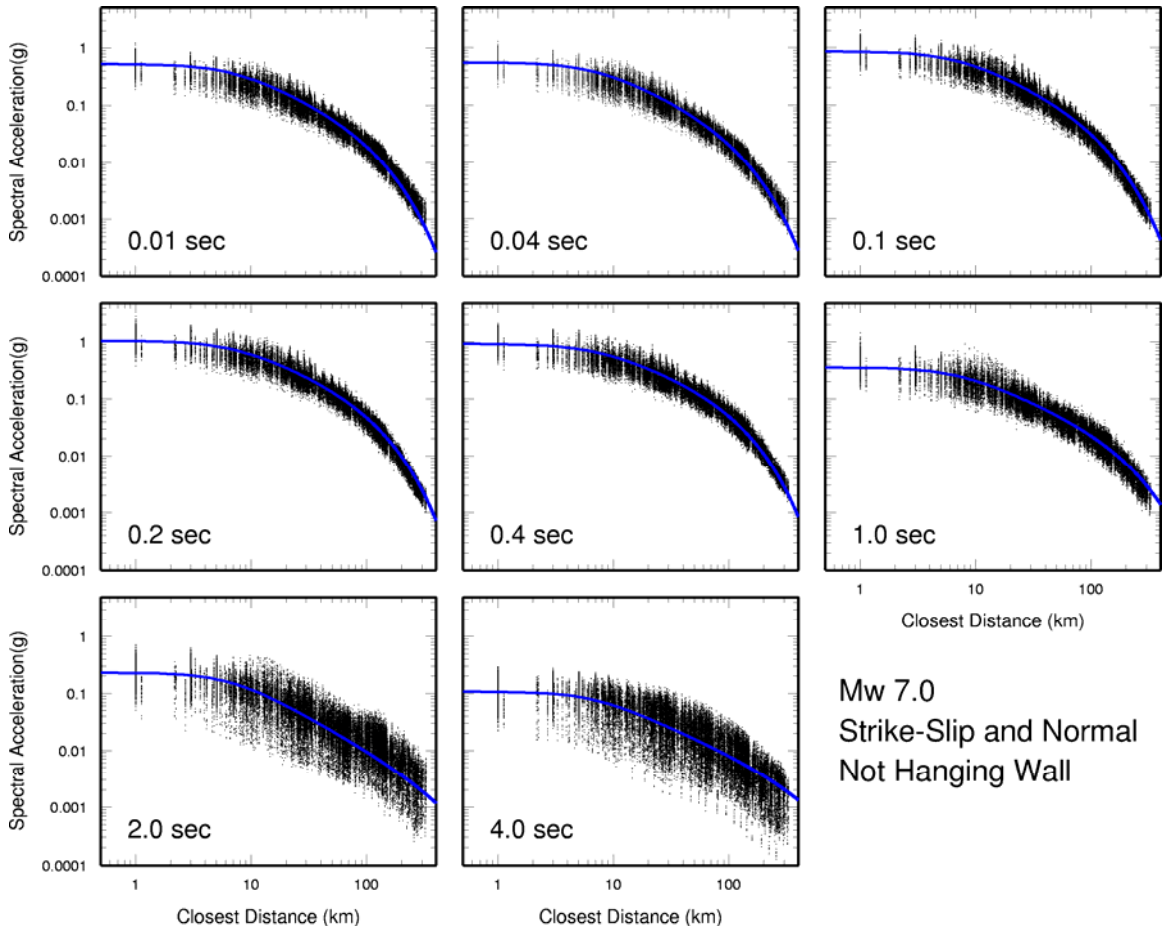

Figure 19. Attenuation of simulated ground motions for magnitude 7.0 strike-slip earthquakes and for non-hanging wall sites in normal faulting earthquakes. The model is shown by the blue line.

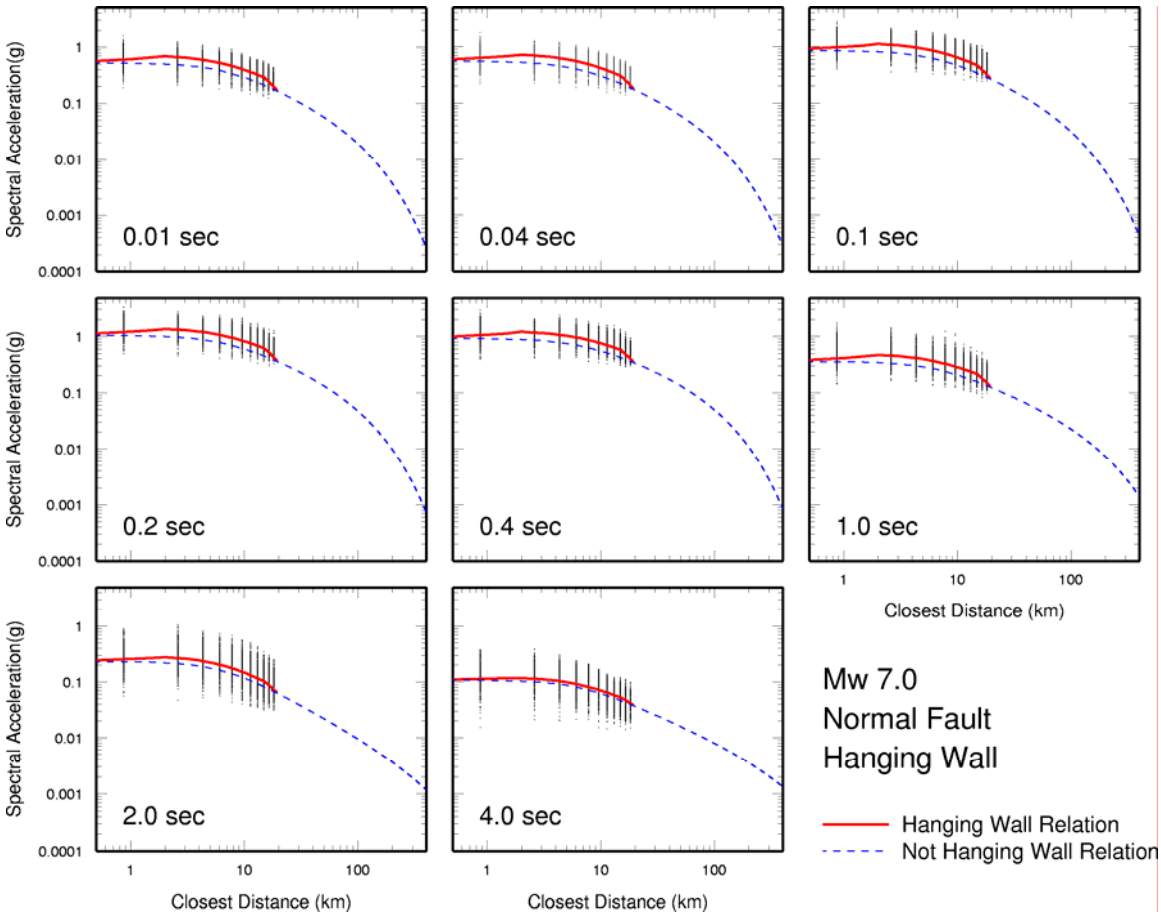

Figure 20. Attenuation of simulated ground motions for hanging wall sites for magnitude 7.0 normal faulting earthquakes. The hanging wall model is shown by the solid red line, and the non-hanging wall model is shown by the dashed blue line. The two models merge at a closest distance of 20 km.

Ground Motion Model Parameterization

Ground motion characteristics depend not only on the seismic moment and distance of the earthquake, as is commonly represented in empirical ground motion attenuation relations, but also on such parameters as the fault orientation, style of faulting, depth of faulting, and the location of the hypocenter and the recording station. Examples of these effects include style of faulting effects, rupture directivity effects (Somerville et al., 1997) and hanging wall effects (Abrahamson and Somerville, 1996). We allowed for differences in ground motions between strike-slip and normal faulting earthquakes in developing the model, but found that the ground motions for strike-slip earthquakes and for non-hanging wall motions for normal faulting earthquakes could be represented by the same model. We developed a separate model for hanging wall motions for normal faulting at closest distances less than 20 km. The strike-slip model is defined for moment magnitudes up to 8, and the normal faulting models are defined for moment magnitudes up to 7.5. The ground motions are for a shear wave velocity of 0.76 km/sec (NEHRP S_B/S_C boundary), corresponding to soft rock and very stiff soil site conditions, which is the reference site condition used in the USGS National Seismic Hazard Maps.

We used the general functional form of the Abrahamson and Silva (1997) model as the starting point for our model development. We used the random effects model of Abrahamson and Youngs (1992) to develop the ground motion model. The functional form of the model, given in Table 7, follows Abrahamson and Silva (1997). The value of the constant pseudo-depth term H was found to be 6.5 km, similar to the Abrahamson and Silva (1997) value of 6.

Table 7. Form of the Ground Motion Attenuation Relations

$Ln(y) = lnSa(g) = c_1 + c_2Mw + c_3ln(rc) + c_4Mwln(rc) + c_5r + c_6(8.5 - Mw)^2 + c_7HW(8.5 - M)$

where

Sa(g) = spectral acceleration in g

r = closest distance to the fault plane

$rc = sqrt(r^2 + H^2)$

H = 6.5 (pseudo depth term)

HW = r/5, r < 5

= 1, 5<=r < 15

= 1 – (r-15)/(20-15), 15<= r <20

= 0, r >=20

DEVELOPMENT OF THE INTERMOUNTAIN WEST GROUND MOTION MODEL

We used simulations for the magnitude range 6.5 to 7.5 to develop the model. Some models (e.g. Abrahamson and Silva, 1997) use different primary magnitude scaling in different magnitude ranges, with larger scaling at smaller magnitudes. The narrow magnitude range of our simulations does not allow us to evaluate this. Instead, we followed the assumption made by most other models that the primary magnitude scaling applies at all magnitudes, and forced all scaling of spectral shape with magnitude to be represented by the c6 term.

Smoothing of Model Coefficients

We smoothed the period dependence of the coefficients in the following sequence. First, we smoothed the magnitude scaling coefficients c2 and c6 which do not interact. These were assumed to be period independent and were set to their values in one step. Coefficient c2 was smoothed by setting the values between 0.01 and 1 second to their average with weights based on the standard error (hereafter called "Weighted Averaging") and those between and 1.0 and 10 seconds to a smooth curve based on the 3 point running average weighted by the variance (hereafter called "Weighted Smoothing"). For coefficient c6 the Weighted Average was found for periods from 0.01 to 0.3 sand 0.75 to 10 seconds. Weighted Smoothing was used for periods between 0.3 and 0.75 seconds.

Next the Weighted Averaging was applied to the c4 term in one step and to the c3 term in the next step. Coefficient c5, which represents the effects of Q, was fixed next by calculating the Weighted Average between 0.01 and 0.04 seconds and between 2.0 and 10 seconds. A line was drawn between these average values at 0.04 and 2.0 seconds and data points linearly interpolated between them.

Finally coefficient c7, which represents the hanging wall effect, was smoothed using the Weighted Average between 0.01 and 1 second and between 3 and 10 seconds and interpolating the value at 2 seconds. The c1 term, which scales the overall level of the ground motions, did not require smoothing. The smoothed coefficients are listed in Table 8, and shown in Figure 21.

Table 8. Coefficients of the Intermountain West Ground Motion Model

Period	C_1	C_2	C_3	C_4	C_5	C_6	C_7
0.01	6.764	-0.758	-1.800	0.1375	-0.0104	-0.236	0.212
0.02	6.761	-0.758	-1.776	0.1357	-0.0104	-0.236	0.212
0.029	6.801	-0.758	-1.780	0.1352	-0.0104	-0.236	0.212
0.04	6.823	-0.758	-1.777	0.1346	-0.0104	-0.236	0.212
0.05	6.887	-0.758	-1.772	0.1314	-0.0104	-0.236	0.212
0.075	7.110	-0.758	-1.743	0.1268	-0.0104	-0.236	0.212
0.10	7.272	-0.758	-1.693	0.1216	-0.0104	-0.236	0.212
0.16	7.376	-0.758	-1.637	0.1203	-0.0104	-0.236	0.212
0.20	7.305	-0.758	-1.597	0.1202	-0.0104	-0.236	0.212
0.24	7.230	-0.758	-1.566	0.1207	-0.0104	-0.242	0.212
0.30	7.183	-0.758	-1.515	0.1156	-0.0104	-0.249	0.212
0.40	7.157	-0.758	-1.435	0.1062	-0.0104	-0.279	0.212
0.50	7.184	-0.758	-1.374	0.0937	-0.0092	-0.311	0.212
0.75	6.919	-0.758	-1.390	0.0926	-0.0070	-0.351	0.212
1.00	6.594	-0.758	-1.480	0.0954	-0.0055	-0.351	0.212
1.40	5.625	-0.646	-1.554	0.0908	-0.0037	-0.351	0.212
2.00	3.014	-0.229	-1.431	0.0465	-0.0018	-0.351	0.153
3.00	0.216	0.125	-1.102	0.0011	-0.0018	-0.351	0.085
4.00	-2.940	0.455	-0.891	0.0000	-0.0018	-0.351	0.085
5.00	-4.598	0.633	-0.827	0.0005	-0.0018	-0.351	0.085
7.50	-5.960	0.681	-0.849	0.0187	-0.0018	-0.351	0.085
10.0	-6.920	0.704	-0.876	0.0305	-0.0018	-0.351	0.085

Table 9. Uncertainty in the ground motion model (natural log units)

Period	Parametric-a	Parametric-b	Modeling	Total
0.01	0.2955	0.39	0.35	0.6016
0.02	0.2916	0.39	0.35	0.5997
0.029	0.2923	0.39	0.35	0.6000
0.04	0.2908	0.39	0.35	0.5993
0.05	0.2940	0.39	0.35	0.6009
0.075	0.2939	0.39	0.35	0.6008
0.10	0.3036	0.39	0.35	0.6056
0.16	0.3075	0.39	0.35	0.6076
0.20	0.3069	0.39	0.35	0.6073
0.24	0.3051	0.39	0.35	0.6064
0.30	0.2977	0.39	0.35	0.6027
0.40	0.2936	0.39	0.35	0.6007
0.50	0.2949	0.39	0.35	0.6013
0.75	0.3107	0.39	0.35	0.6092
1.00	0.3443	0.39	0.35	0.6270
1.40	0.5170	0.39	0.35	0.7361
2.00	0.5776	0.39	0.35	0.7799
3.00	0.5808	0.39	0.35	0.7823
4.00	0.6224	0.39	0.35	0.8136
5.00	0.6360	0.39	0.35	0.8241
7.50	0.6007	0.39	0.35	0.7971
10.0	0.5662	0.39	0.35	0.7715

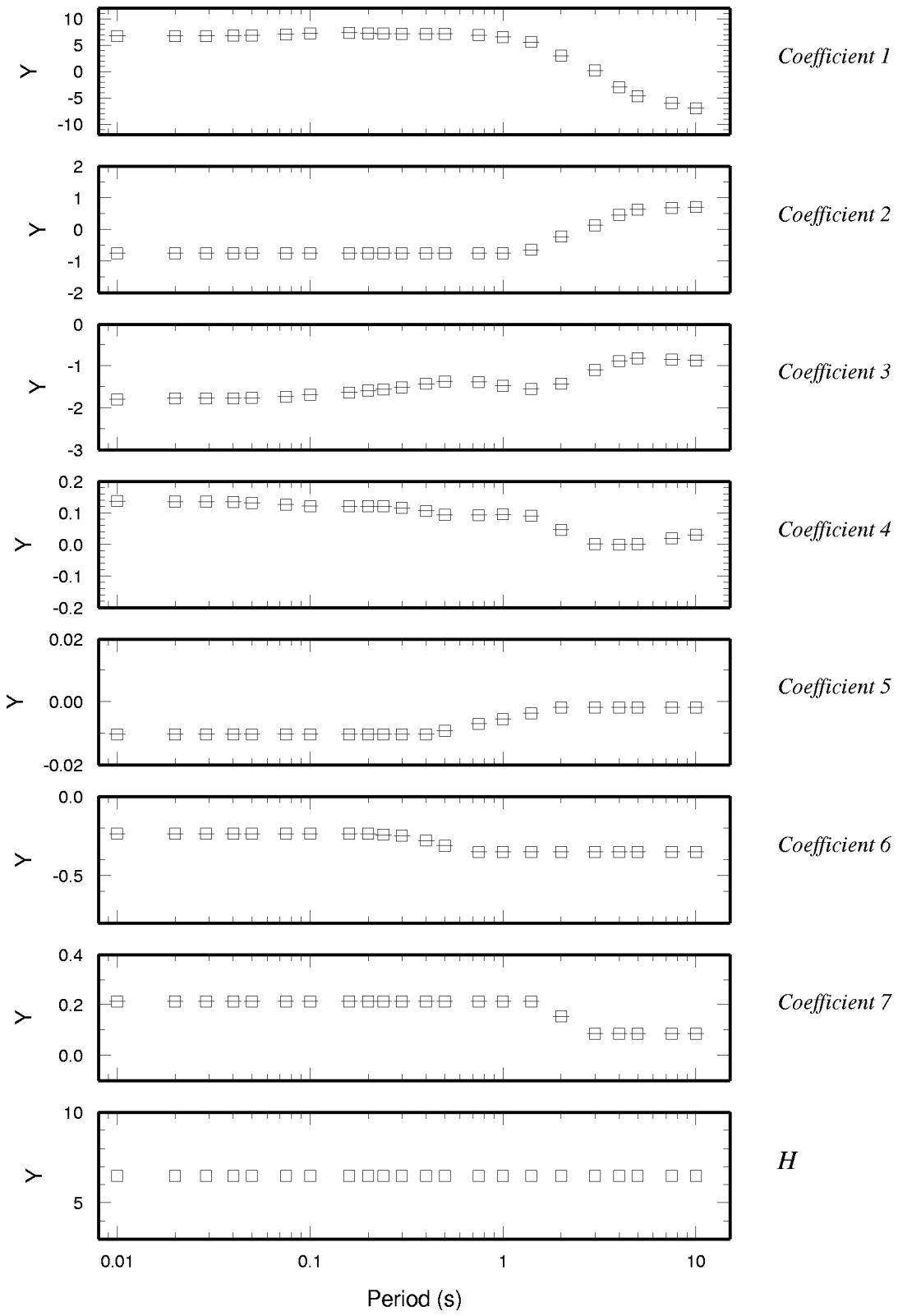

Figure 21. Model coefficients as a function of period.

Representation of Uncertainty in Ground Motions

To be optimally useful in seismic hazard calculations, the attenuation relations need to include comprehensive representation of uncertainty. The parameters that need to be specified include the median value (μ) of the ground motion parameter, the scatter (σ) about the median value, and the uncertainty in each of these two values (σ_μ and σ_σ). The median values are obtained from the equation listed in Table 7 using the coefficients in Table 8. The values of σ_μ and σ_σ are estimated to be 0.2 and 0.15 natural log units respectively, based on our work for the Trial Implementation Project (Savy, 1997).

The variability (σ) of the ground motion model, expressed as the natural logarithm of the standard error, is given in Table 9. The variability was estimated using the procedure described by Abrahamson and Youngs (1992). Two categories of variability are accounted for. Modeling uncertainty, measured by the difference between recorded and simulated ground motions, represents the discrepancy between the actual physical processes and the simplified representation of them in the model. Parametric uncertainty represents the uncertainty in the values of the model parameters in future earthquakes. The total uncertainty is obtained from the combination of these two components.

The estimate of modeling uncertainty used in this project is representative of that obtained from the simulation of recorded strong ground motions of earthquakes in the magnitude range of 6.5 to 7.5 whose source parameters are well known (e.g. Somerville et al. 1996). The modeling uncertainty, which is listed in Table 9, is approximately independent of period.

The estimate of parametric uncertainty was obtained from two sources. One source consists of the parameters that were varied in the simulations performed for this project. These include the distribution of slip on the fault, the location of the hypocenter, the location of the recording station with respect to the fault, and the source depth. The combined contribution of variations in these source parameters is listed under the heading of Parametric-a in Table 9. This component of the parametric uncertainty increases with period, reflecting the transition from more stochastic source and wave propagation effects in the short period component of the simulations, to more deterministic effects in the long period simulations.

The other estimate of parametric uncertainty relates to source parameters that were varied by us in previous studies but not in this study. These parameters include variations in crustal structure, which contribute a standard error of 0.2 natural log units (EPRI, 1993); variations in rupture area for a given seismic moment (static stress drop), which contribute a standard error of 0.28 natural log units (EPRI, 1993); and variations in rise time and rupture velocity, which contribute a standard error of 0.15 and 0.10 natural log units respectively (Otsuka et al., 1998). The combined parametric uncertainty due to variations in these parameters, 0.39 natural log units, is listed in Table 9 under the heading Parametric-b.

The total uncertainty in the ground motion model, listed in the right hand column of Table 9, is obtained by the square root of the sum of the squares (SRSS) combination of all of the above contributions to uncertainty.

DESCRIPTION OF THE INTERMOUNTAIN WEST GROUND MOTION MODEL

We used the procedures described above to develop ground motion models for horizontal ground motions for strike-slip and normal faulting earthquakes. The ground motions are for a shear wave velocity of 0.76 km/sec (NEHRP S_B/S_C boundary), corresponding to soft rock and very stiff soil site conditions, which is the reference site condition used in the USGS National Seismic Hazard Maps. The ground motions for strike-slip earthquakes and for non-hanging wall motions for normal faulting earthquakes are represented by the same model. There is a separate model for hanging wall motions for normal faulting at closest distances less than 20 km. The strike-slip model is defined for moment magnitudes up to 8, and the normal faulting models are defined for moment magnitudes up to 7.5. The coefficients of these models are listed in Table 8, and the standard errors are listed in Table 9.

The attenuation of response spectral acceleration for several periods for magnitudes 5.5 through 8.0 is shown in Figures 22 and 23, which display the strike-slip and non-hanging wall motions and the hanging wall motions respectively. The hanging wall model is higher than the non hanging wall model in the distance range of 5 to 20 km. Figure 24 shows the scaling of response spectra with magnitude for a distance of 10 km, and Figure 25 shows the scaling of response spectra with distance for each of three magnitudes. These two figures are shown using both linear and log axis scales.

The ground motion models have magnitude saturation at short periods at magnitude 7.0. They show a hanging wall effect that decreases with increasing magnitude. The form we have used to represent the magnitude scaling of the hanging wall effect makes it unsuitable for use above magnitude 7.5, where it is undefined by simulations. Normal faulting earthquakes having magnitudes larger than 7.5 are not defined in the current USGS National Seismic Hazard Maps.

The ground motions have large long period amplitudes at close distances from large earthquakes, reflecting forward rupture directivity effects. In this model, we have not attempted to incorporate the spatial dependence of ground motion amplitudes on rupture directivity effects using parameters such as site location with respect to the hypocenter and fault geometry.

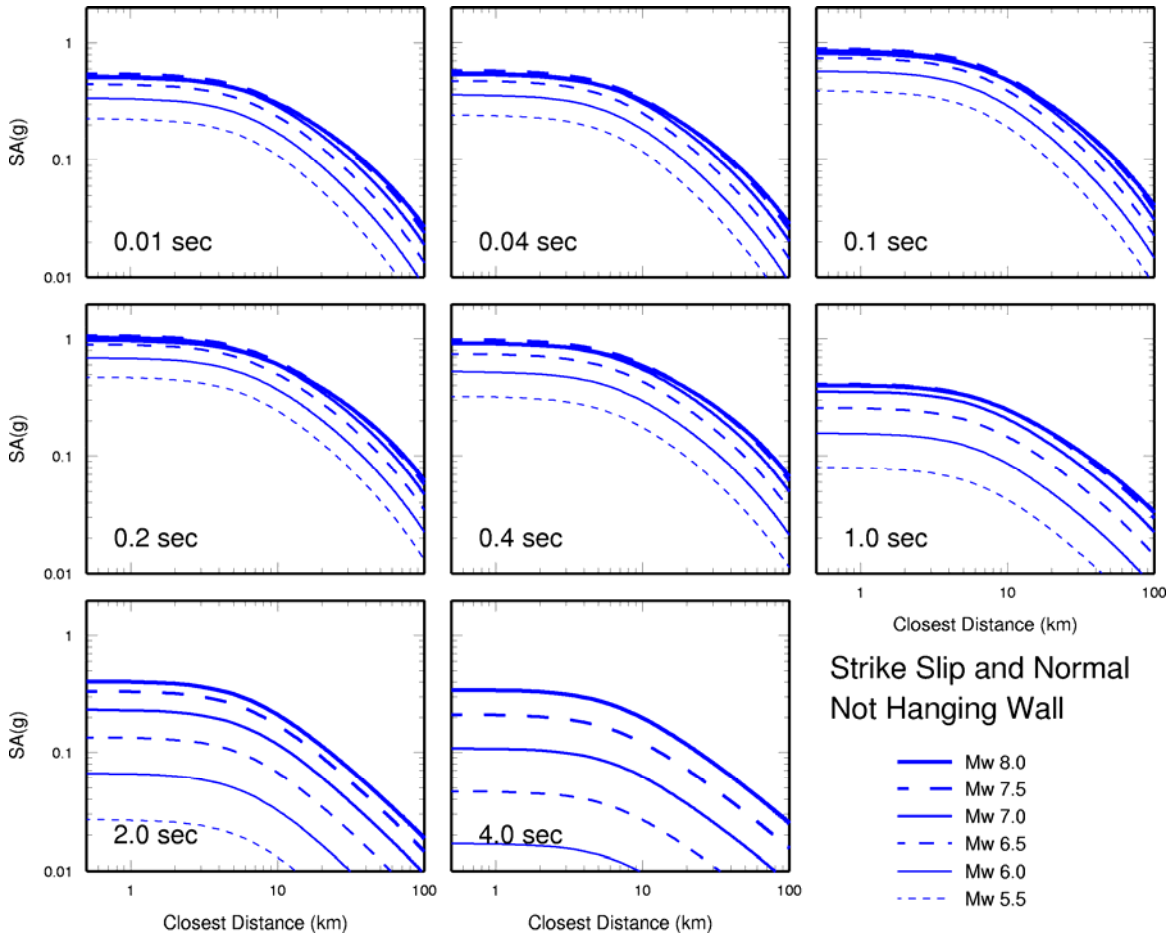

Figure 22. Attenuation for strike-slip and for non-hanging wall sites in normal faulting. The relations for normal faulting are not defined for magnitude Mw larger than 7.5.

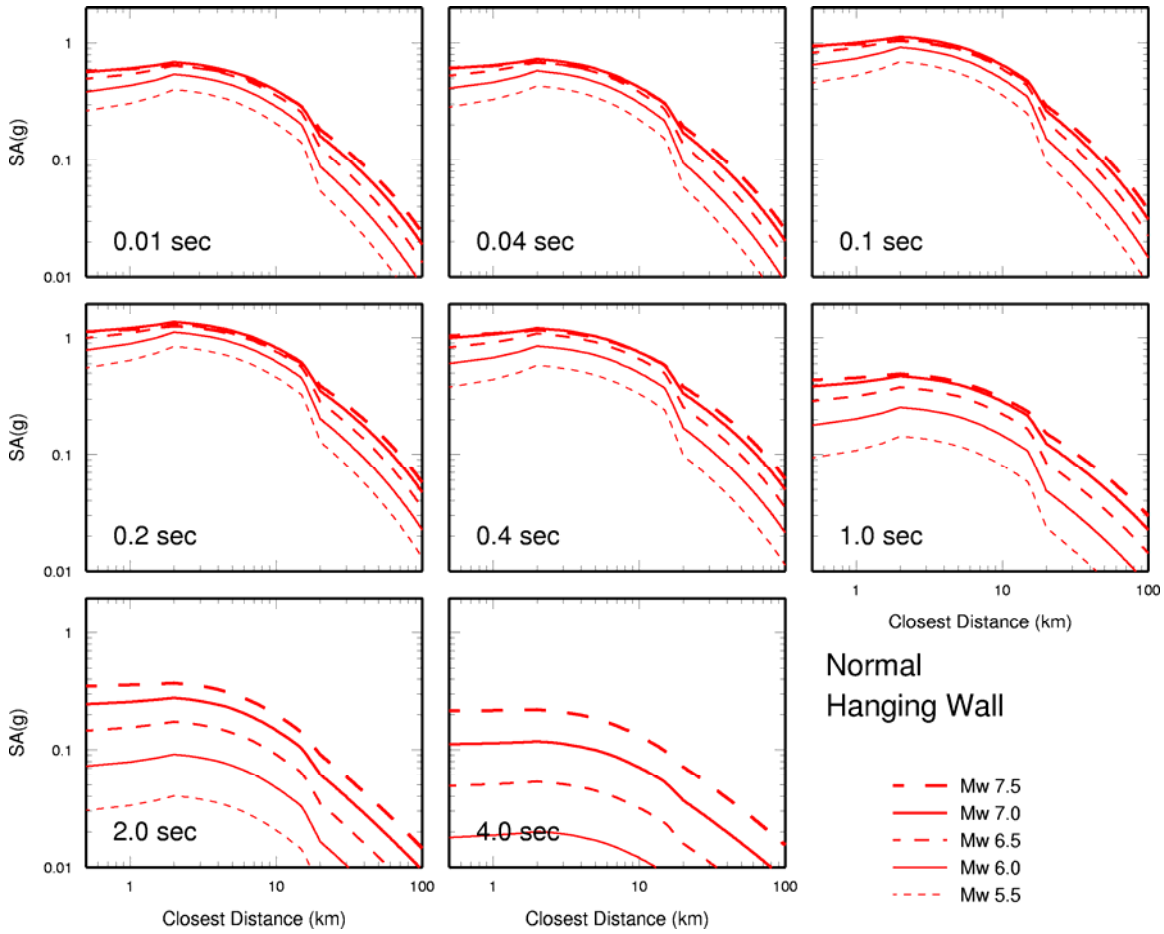

Figure 23. Attenuation for hanging wall sites in normal faulting.

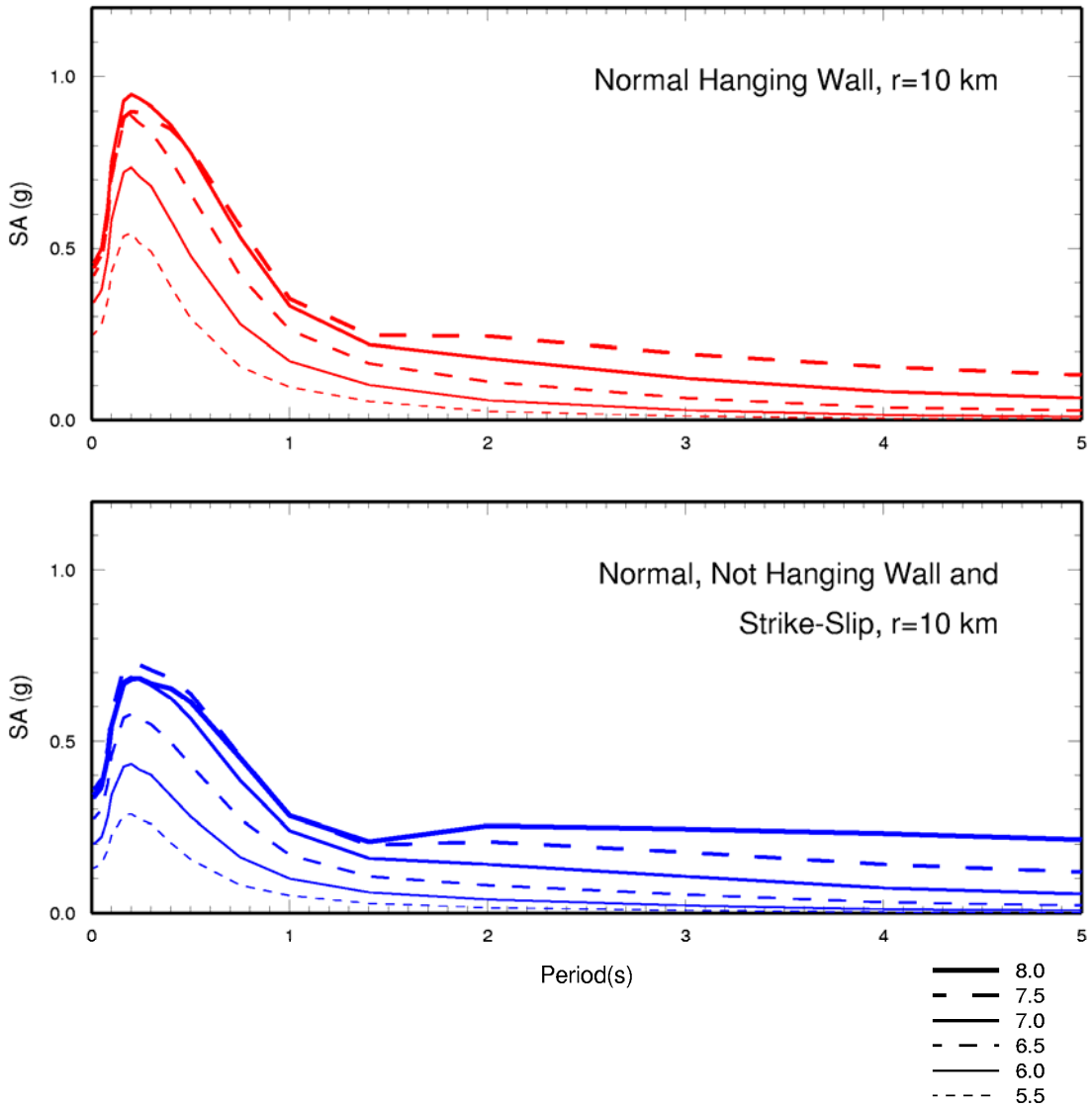

Figure 24a. Magnitude scaling of response spectra for hanging wall sites in normal faulting (top), and for strike-slip and non-hanging wall sites in normal faulting (bottom), linear axis scales. The relations for normal faulting are not defined for magnitude Mw larger than 7.5.

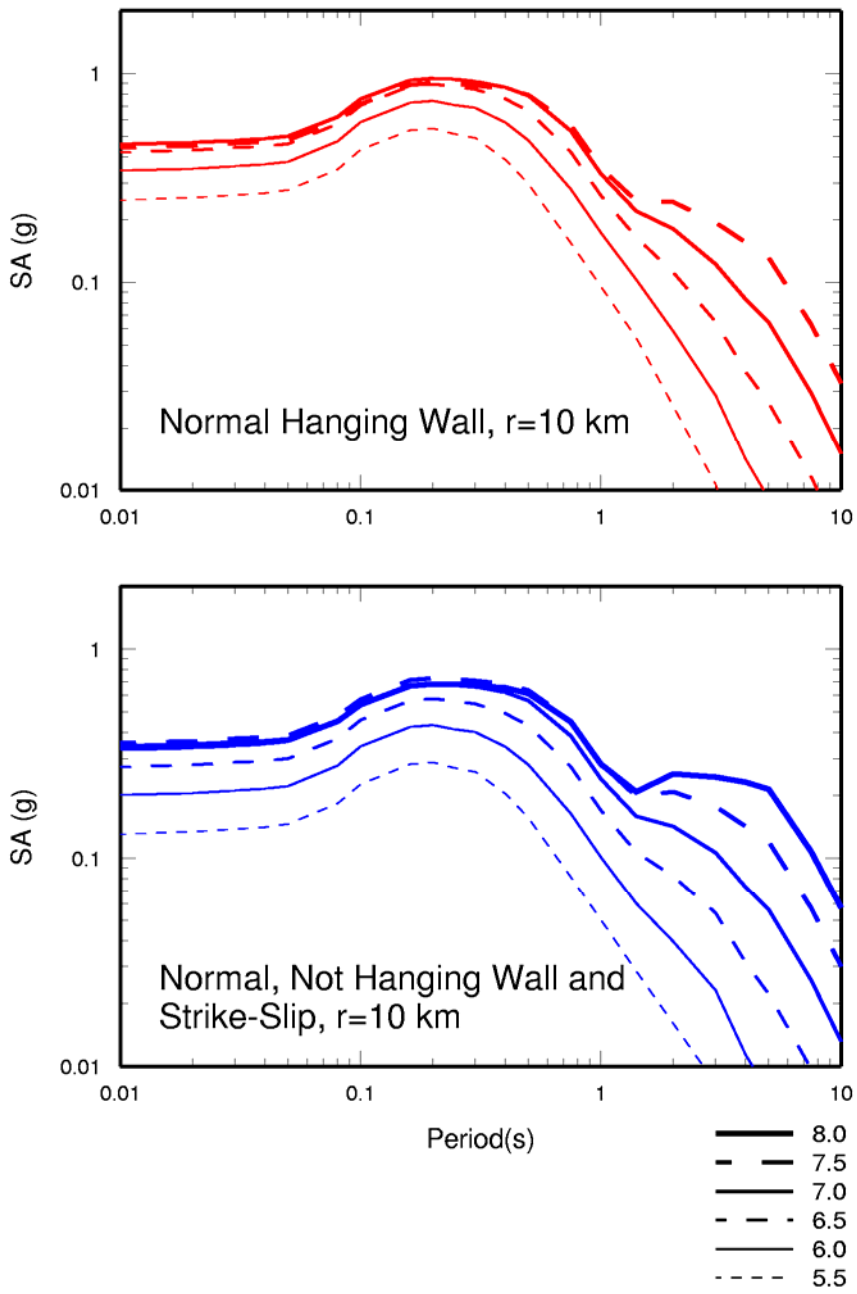

Figure 24b. Magnitude scaling of response spectra for hanging wall sites in normal faulting (top), and for strike-slip and non-hanging wall sites in normal faulting (bottom), log axis scales. The relations for normal faulting are not defined for magnitude Mw larger than 7.5.

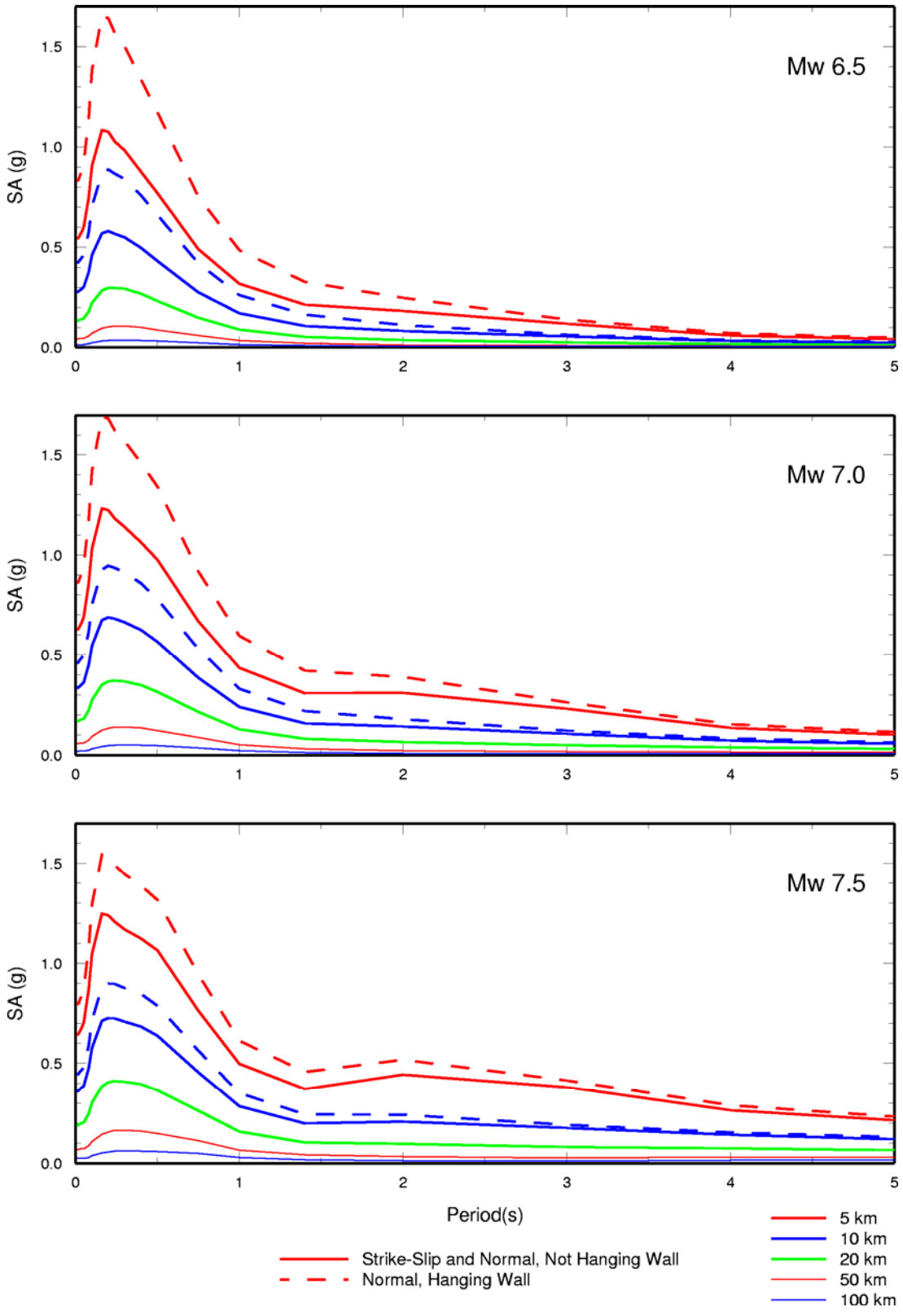

Figure 25a. Distance scaling of response spectra for various magnitudes, linear axis scales. Differences between hanging wall and non-hanging wall sites in normal faulting are limited to closest distances less than 20 km.

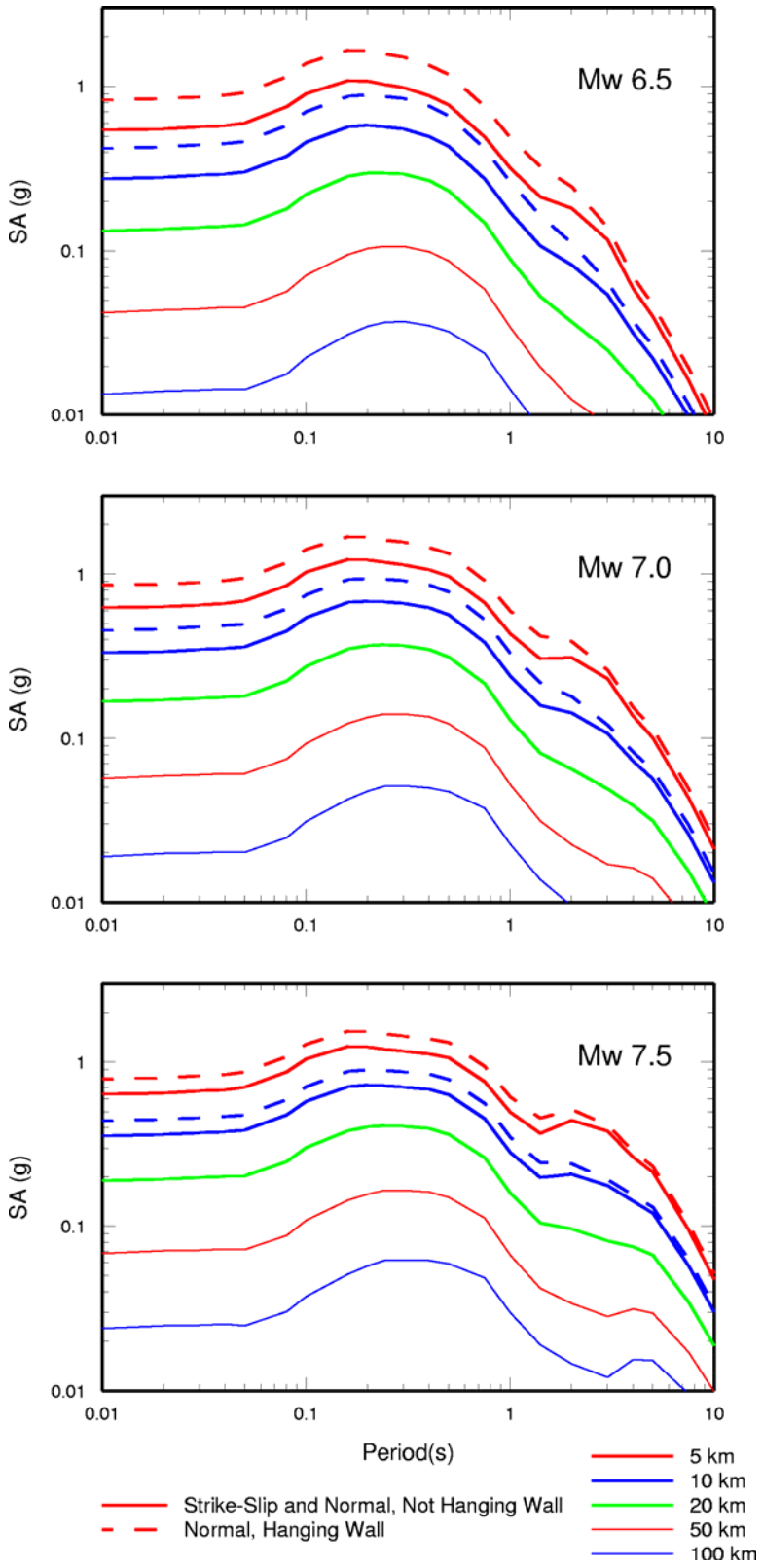

Figure 25b. Distance scaling of response spectra for various magnitudes, log axis scales. Differences between hanging wall and non-hanging wall sites in normal faulting are limited to closest distances less than 20 km.

DISCUSSION

Although the source dimension scaling of normal faulting earthquakes appears to be similar to that of other earthquakes in tectonically active regions, it has been suggested that their ground motions are lower. Spudich et al. (1999) concluded that ground motions from earthquakes in extensional environments are about 10 to 20% weaker than those from strike-slip earthquakes in non-extensional regions of California, indicating that ground motion models derived mainly from California strike-slip data are expected to overpredict ground motions in the Intermountain West. When they compared the ground motions of strike-slip and normal faulting earthquakes in extensional regimes, Spudich et al. (1999) found that strike-slip ground motions were larger than normal faulting ground motions, but by an amount that they considered not to be significant. Our results indicate no significant difference between strike-slip ground motions and non-hanging wall ground motions from normal faulting earthquakes.

Using three-dimensional dynamic simulations on dipping faults that break the surface, Oglesby et al. (2000) showed that the effect of the free surface is to reduce the slip velocity on the shallow part of the fault of normal faulting earthquakes, compared with strike-slip and reverse faulting earthquakes. Shi et al. (2003) obtained qualitatively similar results using a 2D lattice particle model. Also, Brune and Anooshepoor (1999) measured lower near-fault accelerations for normal than for strike-slip faulting in foam rubber, and pointed out that in an extensional faulting regime, the static normal and shear stresses along the fault must approach zero at the surface, so that the upper few km of the fault must store less strain energy than for strike-slip faulting. We have modeled the upper 5 km of the source for both strike-slip and normal faulting earthquakes using low slip velocity and rupture velocity. We do not obtain a significant difference between strike-slip and normal faulting ground motions. We conclude that for both strike-slip and normal faulting, the upper 5 km does not contribute significantly to the strong ground motions.

SUMMARY

We have developed a strong ground motion model for earthquakes in the Intermountain West using a strong motion simulation procedure. The strong motion simulations use earthquake source parameters and scaling relations that are consistent with the source parameters of Basin and Range earthquakes, and Green's functions that are calculated from known crustal structure models of the Intermountain West. The ground motions are for a shear wave velocity of 0.76 km/sec (NEHRP S_B/S_C boundary), corresponding to soft rock and very stiff soil site conditions, which is the reference site condition used in the USGS National Seismic Hazard Maps. We developed models for horizontal ground motions for strike-slip and normal faulting earthquakes. The ground motions for strike-slip earthquakes and for non-hanging wall motions for normal faulting earthquakes are represented by the same model. There is a separate model for hanging wall motions for normal faulting at closest distances less than 20 km. The strike-slip model is defined for moment magnitudes up to 8, and the normal faulting models are defined for moment magnitudes up to 7.5. The ground motion models have short-period magnitude saturation at magnitude 7.0. They show a strong hanging wall effect that decreases with increasing magnitude. The ground motions have high long period amplitudes at close distances from large earthquakes, reflecting forward rupture directivity effects. We have not attempted to incorporate the spatial dependence of ground motion amplitudes on rupture directivity effects using parameters such as site location with respect to the hypocenter and fault geometry.

ACKNOWLEDGMENTS

Research supported by the U.S. Geological Survey (USGS), Department of the Interior, under USGS award number 05HQGR0031. The views and conclusions contained in this document are those of the authors and should not be interpreted as necessarily representing the official policies, either expressed or implied, of the U.S. Government.

REFERENCES

Abrahamson. N.A. and K. Shedlock, 1997. Overview of ground motion attenuation relations. *Seismological Research Letters*, 68: 9-23.

Abrahamson. N.A. and W.J. Silva, 1997. Empirical response spectral attenuation relations for shallow crustal earthquakes. *Seismological Research Letters*, 68: 94-127.

Abrahamson, N.A. and P.G. Somerville (1996). Effects of the hanging wall and footwall on ground motions recorded during the Northridge Earthquake, *Bull. Seism. Soc. Am.,* 86, S93-S99.

Abrahamson, N.A. and R.R. Youngs (1992). A stable algorithm for regression analyses using the random effects model. *Bull. Seism. Soc. Am.,* 82, 505-510.

Becker, A.M. and N.A. Abrahamson (1997). Stress drops in normal faulting earthquakes. *Seismological Research Letters*, 68, 322.

Boore, D.M. (1983). Stochastic simulation of high frequency ground motions based on seismological models of the radiated spectra. *Bull. Seism. Soc. Am.,* 73, 419-434.

Boore, D.M. and W. Joyner (1997). Site amplification for generic rock sites. *Bull. Seism. Soc. Am*., 87, 327-341.

Brune, J.N. (1970). Tectonic stress and the spectra of seismic shear waves from earthquakes. *J. Geophys. Res.* 75, 4997-5009.

Brune, J. N., and A. Anooshehpoor (1999). Dynamic geometrical effects on strong ground motion in a normal fault model. *J. Geophys. Res*., **104,** 809-815**.**

Burger, R.W., P.G. Somerville, J.S. Barker, R.B. Herrmann, and D.V. Helmberger (1987). The effect of crustal structure on strong ground motion attenuation relations in eastern North America, *Bull. Seism. Soc. Am*., **77**, 420-439.

Catchings, R.D. and W.D. Mooney (1991). Basin and Range crustal and upper mantle structure, northwest to central Nevada. *J. Geophys. Res*., **96,** 6247-6267**.**

Chiou, B. et al. (2003). Validation Guidelines for Numerical Simulation of Ground Motion on Rock Conditions. July 10, 2003.

Doser, D.I. (1986). Earthquake processes in the Rainbow Mountain – Fairview Peak – Dixie Valley, Nevada region 1954-1959. *J. Geophys. Res*., **91,** 12572-12586**.**

Electric Power Research Institute (1993). Guidelines for determining design basis ground motions. EPRI TR 102293.

Frankel, A.D., C. S. Mueller, T. P. Barnhard, E. V. Leyendecker, R. L. Wesson, S. C. Harmsen, F. W. Klein, D. M. Perkins, N. C. Dickman, S. L. Hanson, and M. G. Hopper (2000). USGS National Seismic Hazard Maps. Earthquake Spectra 16, 1-21.

Graves, R. and A. Pitarka (2004). Broadband time history simulation using a hybrid approach. Proceedings of the 13th World Conference on Earthquake Engineering, Vancouver, Canada, August 1-6, 2004, Paper No. 1098.

Guatteri, M., P.M. Mai, G.C. Beroza, and J. Boatwright (2003). Strong ground motion prediction from stochastic – dynamic source models. *Bull. Seism. Soc. Am* 93, 301-313.

Hawkins, F.F., R. LaForge, and R.A. Hansen (1986). Seismotectonic study of the Truckee / Lake Tahoe area, northeastern Sierra Nevada, California for Stampede, Prosser Creek, Boca, and Lake Tahoe dams. Seismotectonic Rept. No. 85-4, U.S. Bureau of Reclamation, Denver, Colorado, 1-210.

Hisada, Y. (2001). A theoretical omega-square model considering spatial variation in slip and rupture velocity. *Bull. Seism. Soc. Am*. 91, 651-666.

Horton, S.P., D.M. dePolo, and W.R. Walter (1997). Source parameters and tectonic setting of the 1990 Lee Vining, California, earthquake sequence. *Bull. Seism. Soc. Am*. 87, 1035-1045.

Ichinose, G., P.G. Somerville and H.K. Thio (2005). Rupture process of the 1948 Fukui earthquake (M 7.1) from the joint inversion of seismic waveform and geodetic data. J. Geophys. Res. 110, B05301, doi:10.1029/2004JB003437.

Ichinose, G., K.D. Smith, and J.G. Anderson (1997). Source parameters of the 15 November Border Town, Nevada, earthquake sequence. *Bull Seism. Soc. Am,* 87, 652-667.

Ichinose, G., J.G. Anderson, K.D. Smith, D. DiPolo, R. Schweickert, and M. Lahren (1999). The seismotectonics of the 30 October 1998 Incline Village, Nevada earthquake and its effects. Seismological Research Letters 70, 297-305.

Ichinose, G., J.G. Anderson, K.D. Smith, and Y. Zeng (2003). Source parameters of eastern California and western Nevada earthquakes from regional moment tensor inversion. *Bull Seism. Soc. Am,* 93, 61-84.

Kagawa, T., K. Irikura and P.G. Somerville (2004). Differences in ground motion and fault rupture process between the surface and buried rupture earthquakes. *Earth Planets Space*, 56, 3-14.

Lohman, R.B., M. Simons and B. Savage (2002). Location and mechanism of the Little Skull Mountain earthquake as constrained by satellite radar interferometry and seismic waveform modeling. J. Geophys. Res. 107.

Mayeda, K and W.R. Walter (1996). Moment, energy, stress drop, and source spectra of western United States earthquakes from regional coda envelopes.*J. Geophys. Res*. 101,11,195-11,208.

Oglesby, D.D., R.J. Archuleta, and S.B. Neilson (2000). The three-dimensional dynamics of dipping faults. *Bull. Seis. Soc. Am*. 90, 616-628.

Ohtsuka, H., P.G. Somerville, and T. Sato (1998). Estimation of broadband strong ground motions considering uncertainty of fault parameters, J. Struct. Mech. Earthq. Eng., JSCE, No.584/I-42, 185-200.

Pakiser, L.C. (1989). Geophysics of the Intermontaine system. In *Geophysical Framework of the Continental United States*, Geological Society of America Memoir 172, p. 235-247.

Priestley, K.F., K.D. Smith and R.S. Cockerham (1988). The 1984 Round Valley, California earthquake sequence. Geophys. J. 95, 215-235.

Sadigh, K., C.Y. Chang, J.A. Egan, F. Makdisi, and R.R. Youngs (1997). Attenuation relationships or shallow crustal earthquakes based on California strong motion data. *Seismological Research Letters* 68, 180-189.

Savy, J. (1997). Ground motion attenuation in eastern North America. Section 4.3 of Report on Trial SHAC Methodology Implementation Project, Lawrence Livermore National Laboratory.

Shi, B., J.N. Brune, Y. Zeng, and A. Anooshehpoor (2003). Dynamics of earthquake normal faulting: two-dimensional lattice particle model. *Bull Seism. Soc. Am.,* 93, 1179-1197.

Smith, K.D. and K.F. Priestley (2000). Faulting in the 1986 Chalfant, California, sequence: local tectonics and earthquake source parameters. *Bull. Seis. Soc. Am*. 90, 813-831.

Smith, R.B., W.C. Nagy, K.A. Julander, J.J. Vivieros, C.A. Barker and D.G. Dants (1989). Geophysics and tectonic framework of the eastern Basin and Range – Colorado Plateau – Rocky Mountain transition. In *Geophysical Framework of the Continental United States*, Geological Society of America Memoir 172, p. 205-234.

Somerville, P.G. and A. Pitarka (2006). Differences in earthquake source and ground motion characteristics between surface and buried earthquakes. *Proceedings of the Eighth National Conference on Earthquake Engineering,* San Francisco, California.

Somerville, P.G., R. Graves, A. Pitarka, and N. Collins (2003). Strong Motion Simulations for Phase NGA-E of the Next Generation Attenuation (NGA) Program. Report to SCEC.

Somerville, P.G., N. Collins, N. Abrahamson, R. Graves and C. Saikia (2001). Earthquake source scaling and ground motion attenuation relations for the central and eastern United States. Final Report to the U.S. Geological Survey, Contract No. 99HQGR0098.

Somerville, P.G., K. Irikura, R. Graves, S. Sawada, D. Wald, N. Abrahamson, Y. Iwasaki, T. Kagawa, N. Smith and A. Kowada (1999). Characterizing earthquake slip models for the prediction of strong ground motion. *Seismological Research Letters*, 70, 59-80.

Somerville, P.G., N. Smith, R. Graves and N. Abrahamson (1997). Modification of empirical strong ground motion attenuation relations for the amplitude and duration effects of rupture directivity. *Seismol. Res. Lett*. 68, 199-222.

Somerville, P., C.K. Saikia, D. Wald, and R. Graves (1996). Implications of the Northridge earthquake for strong ground motions from thrust faults, *Bull. Seism. Soc. Am.,* 86, S115 - S125.

Somerville, P.G., N.F. Smith, and R.W. Graves (1994). The effect of critical Moho reflections on the attenuation of strong motion from the 1989 Loma Prieta earthquake, in *"The Loma Prieta, California, Earthquake of October 17, 1989 - Strong Ground Motion,"* U.S. Geological Survey Professional Paper 1551-A, A67-A75.

Somerville, P.G., J.P. McLaren, C.K. Saikia, and D.V. Helmberger (1990). The November 25, 1988 Saguenay, Quebec earthquake: source parameters and the attenuation of strong ground motion. *Bull. Seism. Soc. Am.,* 80, 1118-1143.

Spudich, P., W.B. Joyner, A.G. Lindh, D.M. Boore, B.M. Margaris, and J.B. Fletcher (1999). SEA99: A revised ground motion prediction relation for use in extensional tectonic regimes. *Bull. Seis. Soc. Am*. 89, 70, 1156-1170.

Stepp, J.C., I. Wong, J. Whitney, R. Quittmeyer, N. Abrahamson, G. Toro, R. Youngs, K. Coppersmith, J. Savy, T. Sullivan, and Yucca Mountain PSHA Project Members (2001). Probabilistic seismic hazard analyses for ground motions and fault displacement at Yucca Mountain, Nevada. Earthquake Spectra 17, 113-151.

Thompson, G.A., R. Catchings, E. Goodwin, S. Hollbrook, C. Jarchow, C. Mann, J. McCarthy, and D. Okaya (1989). Geophysics of the western Basin and Range province. In *Geophysical*

Framework of the Continental United States, Geological Society of America Memoir 172, p. 177-204.

Wells, D.L. and K.J. Coppersmith (1994). Analysis of empirical relationships among magnitude, rupture length, rupture area, and surface displacement, *Bull. Seismol. Soc. Am. 84,* 974-1002.